Resolving the Tectonic Stress by the Inversion of Earthquake Focal Mechanisms. Application in the Region of Greece. A Tutorial

Chapter · May 2018
DOI: 10.1007/978-3-319-77359-9_19

2 authors:

Ioannis Kassaras
National and Kapodistrian University of Athens
130 PUBLICATIONS **1,089** CITATIONS

SEE PROFILE

Vasilis Kapetanidis
National and Kapodistrian University of Athens
61 PUBLICATIONS **105** CITATIONS

SEE PROFILE

Resolving the Tectonic Stress by the Inversion of Earthquake Focal Mechanisms. Application in the Region of Greece. A Tutorial

Ioannis G. Kassaras and Vasilis Kapetanidis

Keywords Earthquakes · Active tectonics · Stress tensor · Strain tensor
Moment tensor · Focal mechanism · Inversion · Seismotectonics
Wallace-Bott hypothesis

1 Introduction

This work describes the derivation of the tectonic stress from the inversion of focal mechanisms of double-couple earthquakes. The presented material is based, in large part, on several review papers, lecture notes and practices on the matter, developed by the authors during the last years.

The rupture of geological faults produces the so-called "double-couple" or "tectonic earthquakes" that constitute the major cause of deformation of the Earth's lithosphere. The causes of tectonic earthquakes are forces applied on surfaces (stresses) that drive the earthquake cycle, during which energy is accumulated and released abruptly, generating elastic waves which propagate through the Earth. The analysis of earthquake driving forces is complicated, and their accurate knowledge is a challenging milestone, with numerous applications in geosciences.

Although present-day kinematics of the Earth's surface is efficiently monitored by geodetic remote sensing (GNSS), an accumulation of evidence regarding the earthquake cycle is required, involving the scientific fields of structural geology and seismology. Both provide observations regarding the deformation of the crust, while seismology sets robust constraints on the coseismic stress release within the entire volume of the crust. The most efficient tool in seismology for studying the

I. G. Kassaras (✉) · V. Kapetanidis
Department of Geophysics and Geothermics, National and Kapodistrian University of Athens, Panepistimiopolis, 15784 Zografou, Greece
e-mail: kassaras@geol.uoa.gr

V. Kapetanidis
e-mail: vkapetan@geol.uoa.gr

S. D'Amico (ed.), *Moment Tensor Solutions*, Springer Natural Hazards,
https://doi.org/10.1007/978-3-319-77359-9_19

relative magnitudes and directions of the stresses released during earthquakes is the determination of focal mechanisms.

However, the use of individual focal mechanisms for the assessment of the tectonic stress is not a straightforward solution, since the degree that they sample intrinsic tectonic episodes varies. This is due to several uncertainties related to inherent ambiguities in the definition of the fault plane and slip direction or to the accuracy of the individual focal mechanisms and the respective inversion methods' assumptions. Moreover, the stress field can be heterogeneous, complicated by processes that operate at different 2D/3D spatial scales, which may be a) large, related to plate motion, b) intermediate, reflecting lithospheric flexure/lateral density contrasts (Zoback 1992; Richardson 1992), or c) small, associated with geothermal or hydrocarbon reservoirs (Heidbach et al. 2007). These sorts of processes may be obscured or overestimated by the individual solutions, depending on the available data.

Consequently, individual focal mechanisms should be used with caution and only as a proxy for resolving the tectonic stress (McKenzie 1969; Célérier 2010). As a countermeasure to the above, several methodologies for the determination of the stress field from the inversion of sets of focal mechanism data have been proposed (e.g. Gephart and Forsyth 1984; Gephart 1990; Michael 1984, 1987; Angelier 2002), the application of which has been proven effective for resolving stress at various spatial scales, proportionally to the data multitude and quality (e.g. Zoback et al. 1989; Zoback 1992; Sperner et al. 2003; Heidbach et al. 2010). A largely acknowledged outcome of these concepts and methods is the World Stress Map Project (WSMP, Heidbach et al. 2016), a global compilation of information on the crustal present-day stress field maintained since 2009 at the Helmholtz Centre Potsdam GFZ German Research Centre for Geosciences (http://www.world-stress-map.org).

Apart from the seismic hazard assessment, which is a particular concern, applications of the stress inversion method include: calculation of deviations from the uniform fault motion at a range of spatial and temporal scales related to fault coupling variance, identification of fault zones or segments with significant strain accumulation that have not ruptured in a recent earthquake, migration of stresses, strain deficit etc. Moreover, the method favorably applies to the current needs of the oil industry, such as the exploitation of new, naturally fractured reservoirs. The latter requires knowledge of the present and past stress field and is important for the drilling and borehole stability through the prediction of the orientation of fractures induced by hydraulic fracturing, or "fracking" (Lejri 2015).

The first part of this work invokes the basic theory regarding the fundamentals of stress inversion, while the second presents the application of the method to a comprehensive dataset for Greece (Kassaras et al. 2016a), the most seismically active and tectonically complex region in Europe (SHARE project; Stucchi et al. 2013).

2 Basic Concepts

In seismically active regions, tectonic stress drives the "interseismic" phase, during which energy is accumulated within the rock volume, and the "post-seismic" phase, related to the viscoelastic relaxation of the crust after the abrupt stress release or "coseismic" phase (Bock and Melgar 2016). Tectonic stress is a long-term entity described by a second-order "stress tensor", distinct from the **moment** or **stress release**, represented by the "moment tensor".

2.1 The Stress Tensor

Typical models of tectonic stress are described in terms of forces acting at some distance from the area where a tectonic structure might develop (e.g. Muller and Pollard 1977). In the simplest cases, this distance is assumed to be large with respect to the dimensions of the structure and hence these 'regional' stresses are considered to be homogeneous (Pollard and Saltzer 1993), specified by a single force.

The generalized case of the applied stresses inside a material can be described by a second-order stress tensor σ_{ij}.

$$\sigma_{ij} = \begin{bmatrix} \sigma_{11} & \sigma_{12} & \sigma_{13} \\ \sigma_{21} & \sigma_{22} & \sigma_{23} \\ \sigma_{31} & \sigma_{32} & \sigma_{33} \end{bmatrix} \quad (1)$$

The stresses are applied as coupled forces at opposite sides of an infinitesimal cube and towards opposite directions, cancelling one another to preserve equilibrium, but producing strain. The elements of the diagonal correspond to vectors which are normal to the surface of the cube that is indicated by the first index, i, and responsible for strain that changes the cube's volume. The other, non-diagonal stress elements refer to vectors which are coplanar to the applied surface and can cause shape-changing shear strain to the cube. In the literature, the latter are sometimes represented by τ_{ij} ($i \neq j$), to distinguish between normal and shear stresses.

The elements of the stress tensor depend on the coordinate system that is chosen; the orientation of the infinitesimal cube with respect to the stress field. The stress tensor is a diagonalizable matrix, which means it can be rotated to a specific coordinate system where its non-diagonal elements (shear stresses) become zero. In that system, the only stresses acting on the cube are oriented in directions indicated by the cube's normal vectors, called principal stress axes. The directions, $\mathbf{S}_1$, $\mathbf{S}_2$, $\mathbf{S}_3$, and magnitudes, σ_1, σ_2 and σ_3, of the principal stresses can be derived from the eigenvectors and eigenvalues of the stress tensor, respectively. Eigenvalues are real numbers that represent the magnitude of the principal stresses while eigenvectors define their geometry. In geological applications where the stresses are all nega-

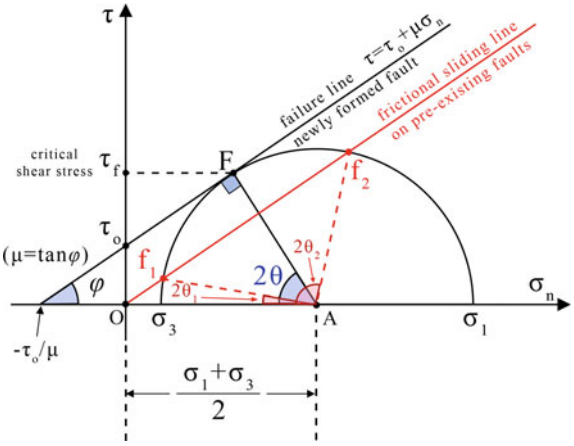

Fig. 1 Mohr's circle for the definition of frictional slide on pre-existing faults (red line) or failure angles on newly formed faults (black line parallel to the red one), where φ is the angle of internal friction, θ is the angle between the $\mathbf{S}_1$ axis and the failure plane, σ_n is the applied normal stress, τ is the applied shear stress, τ_o the cohesive strength and $(-\tau_o/\mu)$ the tensile strength of the material. The circle's radius is AF = $(\sigma_1 - \sigma_3)/2$, that is also the value of maximum shear stress for $\theta = 45°$ (if $\varphi = 0$) (Figure after Kapetanidis 2017)

tive (compressive) they are usually sorted by order of decreasing absolute values $|\sigma_1| \geq |\sigma_2| \geq |\sigma_3|$ (Stein and Wysession 2003).

In the general case, however, the shear stresses are non-zero. Shear stresses inside a material can produce rupture when the applied forces surpass the material's strength. Intuitively, for a given stress field, the material is more likely to break at a surface that is oriented in such a way that the shear stresses maximize. This condition occurs when the principal axes $\mathbf{S}_1$ and $\mathbf{S}_3$ are at a 45° angle from the weak plane (Stein and Wysession 2003).

However, as Reches (1987) notes, slip occurs when Coulomb's failure criterion is fulfilled, i.e. when the shear stress, τ, exceeds frictional resistance:

$$\tau = \tau_o + \mu \cdot \sigma_n \tag{2}$$

where τ_o is the cohesive strength of the rock, or simply cohesion, $\mu = \tan\Phi$ (Fig. 1) is the coefficient of internal friction of the material and σ_n in this formula is considered positive for compression (Scholz 2002). In this more realistic model, the angle θ between the $\mathbf{S}_1$ axis and the failure plane also depends on the angle of internal friction, φ, of the material:

$$\theta = 45° - \varphi/2 \tag{3}$$

When the material contains weak discontinuities, e.g. pre-existing fractures that have been cemented, where the cohesive strength of the material is $\tau_o \approx 0$, frictional

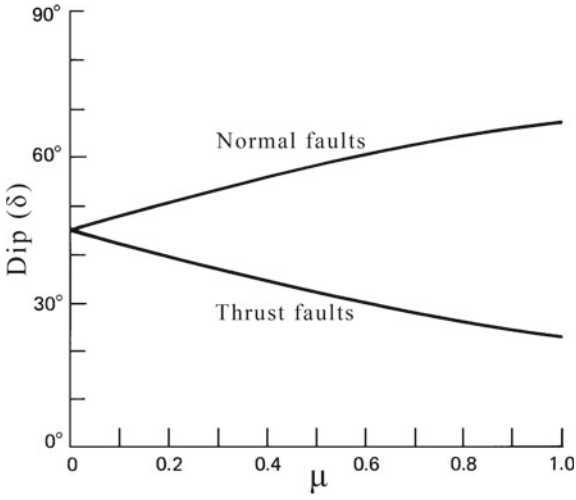

Fig. 2 Relation between the expected fault dip angle, δ, for a given coefficient of internal friction, μ, for normal and thrust faults (Figure after Turcotte and Schubert 2002)

slide can occur for a given stress state if discontinuities are found at either of two preferred orientations, θ_1 and θ_2 (Fig. 1).

The orientation of the maximum and minimum principal stresses, $\mathbf{S}_1$ and $\mathbf{S}_3$, in a regional scale largely defines the expected tectonic regime. When $\mathbf{S}_1$ is sub-vertical and $\mathbf{S}_3$ is sub-horizontal, extension occurs, creating normal fault systems under the vertical lithostatic pressure ($\mathbf{S}_1$). When the contrary is true, thrust faulting occurs under compression imposed by the sub-horizontal $\mathbf{S}_1$. Lastly, when both $\mathbf{S}_1$ and $\mathbf{S}_3$ are subhorizontal, strike-slip faulting takes place. Furthermore, this has implications on the expected dip angles, δ, that normal and thrust faults are likely to occur, depending on the coefficient of internal friction, μ, as calculated in a simple model by Turcotte and Schubert (2002) (Fig. 2).

2.2 The Moment Tensor

Contrary to the tectonic stress, the earthquake rupture cannot be described by a single force, only applicable to certain types of sources, i.e. those related to the collapse of a cave's ceiling. The model of "single-couple" source, with a pair of opposite forces applied at the two walls, parallel to the fault plane, although intuitively valid and correctly reproducing the P-wave radiation pattern, fails to produce the observed polarities and amplitudes for the generated shear waves (Aki and Richards 2002).

To describe the earthquake rupture, Vvedenskaya (1956) introduced the concept of the double-couple, a system of exerting forces at a point of a fault surface, the so-called "*point-source double-couple*", consisting of two opposing torques with equal moment (M_0) imposing volumetric and shear deformation of the elastic medium, with the assumption that translation and rotation are negligible. Thereafter, the *double-*

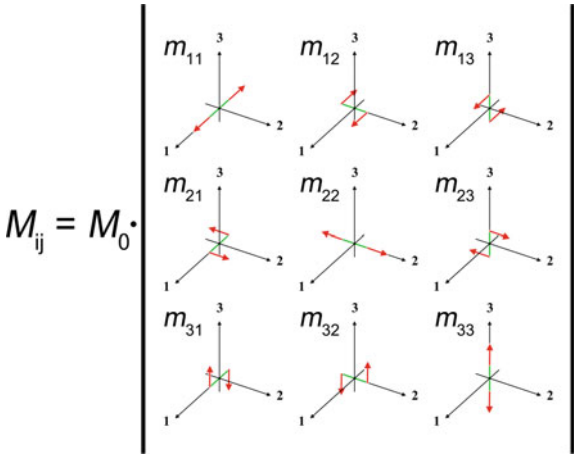

Fig. 3 The components of a Cartesian moment tensor

couple (DC) source model has been widely adopted as adequately explaining sources of tectonic origin, known as double-couple earthquakes. It also correctly predicts the radiation pattern of the shear-waves, as opposed to the single-couple model.

The **Moment Tensor** (MT) is a physical entity that defines the magnitude of a seismic source in terms of its seismic moment, M_0, and the radiation pattern of the recorded seismic waves, i.e. the characteristics of the seismic energy's distribution. A force couple m_{ij} in a Cartesian coordinate system is defined as a pair of opposing forces pointing in the direction of the component indicated by i and separated in the respective j direction (Fig. 3). The acting pairs of forces and torques applied on a point-source are represented by a second-order tensor, i.e. a 3×3 matrix, M_{ij}. The magnitude of M_{ij} is given by the scalar seismic moment M_0, which is defined as the largest singular value of the moment tensor. The diagonal elements in the matrix represent linear vector dipoles; the off diagonal elements represent shear force couples with non-zero torque.

As a second order 3×3 tensor, the MT (Fig. 3) has several similarities to the stress tensor, although the forces described in the former are not acting on infinitesimal surfaces, but rather on points at an infinitesimal distance from the point-source. The elements on its diagonal act as linear dipoles and produce volumetric changes (explosion, implosion and/or tensile fracturing) when the trace is non-zero. Removing the trace from the diagonal leaves behind the deviatoric part of the MT. The latter can still be divided into a pure DC component and another that is called a Compensated Linear Vector Dipole (CLVD). The CLVD component could be significant in earthquakes of volcano-tectonic origin, related to magma inflation or propagation through dykes, fissure eruptions, crack opening or closing without volume changes etc. DC earthquakes, on the other hand, are related to purely tectonic movements. Figure 4 illustrates the representation of a rupture (Fig. 4a) by the DC source model (Fig. 4b). The one couple of forces is acting parallel to the fault plane, defined by its

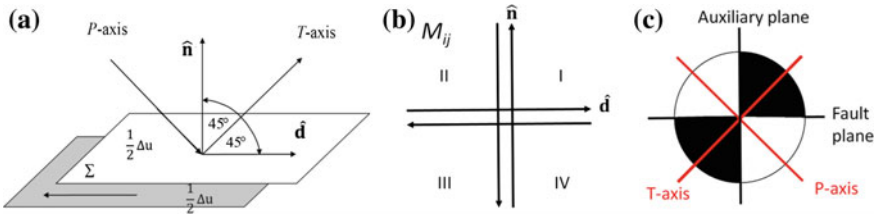

Fig. 4 **a** Dislocation on a fault surface (Σ). The total slip Δu is the difference between the displacements at the hanging-wall and the footwall (modified after Aki and Richards 2002). **b** "Double-couple" force system, equivalent to the dislocation model of panel (**a**) when in equilibrium state. **c** Beachball representation of the P-wave radiation pattern of the models shown in panels (**a**) and (**b**). Black and white quadrants correspond to compressional and dilatational first motion while they also contain the tension (**T**) and compression (**P**) axes, respectively, at 45° from the fault and auxiliary planes

normal vector $\hat{\mathbf{n}}$, and the other parallel to an "auxiliary plane" that is normal both to the fault plane and to the slip vector, **d**.

The unitary vectors $\hat{\mathbf{n}}$ and **d** are related in a way similar to how the stress tensor produces the traction $\hat{\mathbf{t}}$ from the normal vector $\hat{\mathbf{n}}$:

$$\mathbf{d}\left(\hat{\mathbf{n}}\right) = (M_{ij})\hat{\mathbf{n}} \tag{4}$$

The condition that angular momentum be conserved in equilibrium requires that the moment tensor is symmetric ($M_{ij} = M_{ji}$) to prevent rotation, thus leaving 6 independent elements (or 5, if the trace is zero):

$$M_{ij} = M_0\left(\hat{d}_i\hat{\mathbf{n}}_j + \hat{\mathbf{n}}_i\hat{d}_j\right) \tag{5}$$

Interchangeability of $\hat{\mathbf{d}}$ and $\hat{\mathbf{n}}$ in the DC model makes the tensor symmetric ($M_{ij} = M_{ji}$). Practically, this shows that slip on either the fault or the auxiliary plane in the directions indicated by $\hat{\mathbf{d}}$ or $\hat{\mathbf{n}}$, respectively, yields the same seismic radiation pattern, which leads to an inherent ambiguity, contrary to the single-couple model where the fault plane is unambiguously defined. In terms of the radiation pattern, this can be seen in Fig. 4c, where in quadrants I and III (black) the radiated (P-wave) first motion is compressional, or "thrusting away" from the source, while in quadrants II and IV (white) the first motion is dilatational, or "pulling towards" the source.

Another common characteristic between moment- and stress-tensors is that they are both diagonizable. They can be rotated to a common coordinate system which can be expressed as a product with a transformation matrix **A** or **B**:

$$M'_{ij} = A(M_{ij})\mathrm{A}^T, \quad \sigma'_{ij} = B\left(\sigma_{ij}\right)B^T \tag{6}$$

In a pure-DC moment tensor, its diagonalizable form would have two elements with equal value and opposite sign, related to the bisectors $\mathbf{T} = \frac{1}{\sqrt{2}}\left(\hat{\mathbf{d}} + \hat{\mathbf{n}}\right)$ and $\mathbf{P} = \frac{1}{\sqrt{2}}\left(\hat{\mathbf{d}} - \hat{\mathbf{n}}\right)$ (Fig. 4), which represent the axes of tension and pressure, or rather minimum and maximum compressive stress, respectively. Since the trace of M_{ij} (isotropic component) is zero (i.e. the $\hat{\mathbf{d}}$ and $\hat{\mathbf{n}}$ are orthogonal), the third element of the diagonal (or third eigenvalue) would be zero and correspond to the eigenvector in the direction of the intersection of the nodal planes $\mathbf{N} = \left(\hat{\mathbf{d}} \times \hat{\mathbf{n}}\right) = \mathbf{T} \times \mathbf{P}$, where no motion occurs (null axis; sometimes also symbolized as **B**).

The principal axes **P**, **N, T** of the moment tensor fully describe the dynamics and kinematics of a DC point source and are independent of the choice of the two nodal (fault and auxiliary) planes. They can be determined through the eigenvalue and eigenvector analysis of the moment tensor (M_{ij}), similar to the principal stresses $\mathbf{S}_1$, $\mathbf{S}_2$, $\mathbf{S}_3$ and their magnitudes σ_1, σ_2 and σ_3 for the stress tensor, which are related to **P**, **N** and **T**, respectively.

However, the **P**- and **T**-axes are always at a 45° angle from both the fault and the auxiliary planes, while the same is true for $\mathbf{S}_1$ and $\mathbf{S}_3$ only in case of new fracture generation in a homogeneous isotropic medium (e.g. Vavryčuk 2015). Hence, the moment tensor's principal axes **P**, **N**, and **T** do not always correspond to the respective principal stress axes $\mathbf{S}_1$, $\mathbf{S}_2$, and $\mathbf{S}_3$, because earthquakes typically occur on pre-existing faults in a heterogeneous anisotropic medium such as the crust (e.g. Scholtz 2002; Stein and Wysession 2003), due to directional differences caused by the fault shape, fault maturity and frictional anisotropy (Pollard and Saltzer 1993). However, $\mathbf{S}_1$ and $\mathbf{S}_3$ are expected to lie within the same quadrants as **P** and **T**, respectively (Fig. 4).

Inversely, in some methodologies (Vavryčuk 2015) the principal fault planes are considered those which are at an angle of less than 45° from the $\mathbf{S}_1$ axis. In Western Greece, it has indeed been observed that the $\mathbf{S}_1$ axis is usually at a ~30° angle from the principal fault planes (Kassaras et al. 2016b). Various methods have been devised for automatically choosing the fault plane (Lund and Slunga 1999), including the "Slip Angle Method" (e.g. Gephart and Forsyth 1984), which considers the nodal plane that has the smallest misfit between the predicted and observed slip vector orientation and the "Instability Method", which considers the most unstable plane as the one that slips (Lund and Slunga 1999).

In a fault-related earthquake, the DC component of the moment tensor can describe the orientation of the causative fault (its strike, φ_{f}, and dip angle, δ), the direction of the slip on its plane (rake angle, λ) and the magnitude of the rupture (expressed in the form of the released seismic moment, M_{o}), albeit with an ambiguity between the two nodal planes (fault and auxiliary). The elements of the moment tensor in a DC source can be directly calculated from the φ_{f}, δ, λ parameters and vice versa (Aki and Richards 2002; Gasperini and Vannucci 2003). The type of faulting for a certain set of φ_{f}, δ, λ parameters, when they correspond to the fault plane rather than the auxiliary one, can be determined by the value of λ, with $\lambda \approx -90°$ corresponding to normal faulting, $\lambda \approx 90°$ related to reverse faulting and $\lambda \approx 0°$ or $\pm 180°$ associated

Table 1 Stress regime characterization based on the plunge, γ_i, of **P**, **N** and **T** axes (on the basis of them being an approximation of the principal stress axes $\mathbf{S}_1$, $\mathbf{S}_2$ and $\mathbf{S}_3$), where NF, SS and TF refer to normal, strike-slip and thrust faulting, while NS and TS to oblique normal and thrust faulting, respectively. Symbols γ and α refer to the plunge and trend, respectively. The trend of the maximum horizontal stress axis, $\mathbf{S}_{\mathrm{Hmax}}$, is also indicated (after Zoback 1992). The last two lines ("Odd", or "Unknown" faulting type) have been added for completeness

P (σ_1)	N (σ_2)	T (σ_3)	Regime or faulting type	S_{Hmax} trend
$\gamma_P \geq 52°$		$\gamma_T \leq 35°$	NF	α_N
$40° \leq \gamma_P < 52°$		$\gamma_T \leq 20°$	NS	$\alpha_T + 90°$
$\gamma_P < 40°$	$\gamma_N \geq 45°$	$\gamma_T \leq 20°$	SS	$\alpha_T + 90°$
$\gamma_P \leq 20°$	$\gamma_N \geq 45°$	$\gamma_T < 40°$	SS	α_P
$\gamma_P \leq 20°$		$40° \leq \gamma_T < 52°$	TS	α_P
$\gamma_P \leq 35°$		$\gamma_T \geq 52°$	TF	α_P
$40 \leq \gamma_P \leq 50°$	$\gamma_N \approx 0°$	$40 \leq \gamma_T \leq 50°$	"Odd"	–
$25 \leq \gamma_P \leq 45°$	$25 \leq \gamma_N \leq 45°$	$25 \leq \gamma_T \leq 45°$	"Odd"	–

with sinistral or dextral strike-slip faulting, respectively. However, the faulting type represented by a certain DC moment tensor can also be determined by the orientation of its eigenvectors, **P**, **N** and **T**, in a sense which may apply to the characterization of the stress regime in an area. Zoback (1992) determined a set of rules for the classification of faulting type depending mainly on the plunge angles, γ, of the **P** and **T** axes, complemented, in some cases, by the respective plunge of the **N** axis (Table 1). These also determine the trend of the maximum horizontal stress axis, $\mathbf{S}_{\mathrm{Hmax}}$. There is a region of **P** and **T** plunges (γ_P and γ_T) in which focal mechanisms are not classified in a typical faulting type, but rather as "odd" or "unknown". This is the case of either sub-horizontal faults with horizontal slip or sub-vertical faults with (nearly vertical) dip-slip (both γ_P and $\gamma_T \approx 45°$ or all three axes with $25° < \gamma < 45°$). Such cases are generally rare and may characterize very low-angle normal faults or thrusts where the principal stress field is tilted out of horizontal and vertical planes (Zoback 1992). An additional set of criteria for faulting classification (e.g. Milano and Di Giovambattista 2011) can be used to further limit the zone of the "Odd" type.

2.3 Methods to Determine Focal Mechanism Solutions (FMS)

Nowadays, Focal Mechanism Solutions (FMS) are routinely obtained through the analysis of waveform recordings from modern deployments. Methods for determining FMS are based on the observed radiation pattern of seismic waves that depends on the location and orientation of the active fault and slip direction with respect to

the receivers. The most widely applied methods include the determination of FMS through the distribution of first motion polarities of the P-waves (e.g. Kassaras et al. 2014a), polarization and amplitude of the S-waves (e.g. Bernard and Zollo 1989), S/P (or other types of waves) amplitude ratio (e.g. Godano et al. 2014) and moment tensor inversion using body-wave modeling (e.g. Kapetanidis et al. 2015). The solution determined by the latter is known as Moment Tensor Solution (MTS) and it is considered as the most reliable seismological method for defining the rupture dynamics and kinematics.

A variation of MTS, the Centroid Moment Tensor (CMT; http://www.globalcmt.org), includes additional inversion for the source origin time and location, in terms of the centroid of moment release (or slip) as opposed to the hypocenter, which is defined as the location where rupture began (nucleation point). The centroid location for very large earthquakes may significantly differ from the hypocenter; the offset of the centroid relative to the hypocentral location gives a first indication on the fault's extent and directivity of the rupture (Dahm and Krüger 2014). A sound example is the case of the August 17th, 1999 Izmit (Turkey) earthquake, where the centroid (quick CMT solution) was resolved about 30 km east of the epicenter, as determined by the arrival times of seismic waves (Tibi et al. 2001), and coincided with the area where the maximum surface ruptures were observed.

The FMS of tectonic earthquakes can be easily reconstructed from the analysis of the polarities and amplitudes of the P-wave onsets, which can be complemented by the amplitudes of the first arrival of S-waves. However, this must be performed at an adequate number of seismological stations distributed along a wide range of azimuths and for seismic rays at various angles of emergence. Such methods are sufficient to describe the mechanics of tectonic processes within the Earth's crust, mainly at small (local) epicentral distances, using up-going seismic rays, and assuming net slip on the fault (i.e. pure DC source).

Typically, FMS are displayed graphically by the so-called "*beachball*" diagram (Figs. 4c and 5), which gives a sense of the orientation of the nodal planes and the respective direction of the slip vector (for the nodal plane that corresponds to the fault), quadrants of alternating P-wave polarities and orientation and plunge of the **P**, **N** and **T** axes.

For a more detailed analysis of intrinsic geological, mineralogical and other processes, additional information can be derived from the Moment Tensor Solution (MTS) by inversion of seismograms at local, regional or teleseismic distances. The MTS uses the radiation pattern of body waves (e.g. Herrmann and Ammon 1997), surface waves (e.g. Aki and Patton 1978) and normal modes of the free oscillations of the Earth for very large earthquakes (e.g. Bogiatzis and Ishii 2014). MTS involves finding the moment tensor M_{ij} that produces synthetic waveforms which best match the observed seismograms in a least squares sense (e.g. Dahlen and Tromp 1998). Inversion for a full (unrestricted) moment tensor may result in various types of seismic sources (i.e. isotropic, tensile, CLVD, double-couple and their combinations), which is useful when a complex wavefield is involved, related to deep earthquakes, volcanic earthquakes, landslides, nuclear tests, etc. However, the non-DC component (e.g. isotropic and/or CLVD) of earthquake FMS, especially in

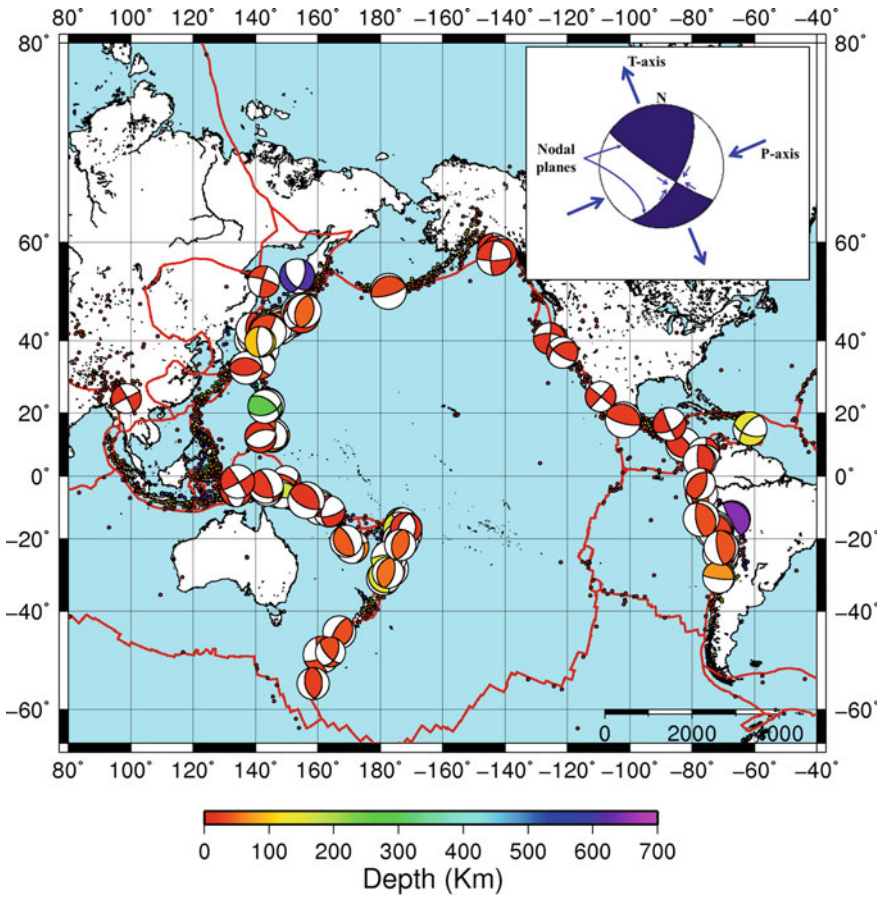

Fig. 5 CMT solutions of earthquakes with $M_w \geq 6.5$ (http://www.globalcmt.org). The "*beachball*" diagram in the upper right shows the stereographic projection of the lower hemisphere of a focal mechanism solution. White quadrants represent dilatational first motion and contain the maximum compression axis, **P**, while dilatational quadrants containing the maximum extension axis (**T**) are presented in color

non-volcanic regions, is usually attributed to noise and/or unmodeled structures in the Earth model employed for calculating Green's functions, in order to produce synthetic seismograms at selected frequency bands.

The quality of either solution, as determined by moment tensor inversion or first-motion analysis, depends not only on the datasets and a typical error estimation but, also, on several additional factors. Dufumier and Cara (1995) and Dufumier (1996) provide a systematic overview of how FMS are affected by the geographical coverage of stations, the type and quantity of the seismic waves involved (P, S, SH, SV), the signal-to-noise-ratio of the waveforms, site-effects and the knowledge of the Earth's structure. Moreover, methodological limitations due to different approaches

and the choice of inversion parameters may strongly impact the solution of the moment tensor inversion. For example, the selection of frequency bandwidth in the waveform recordings can play a major role, with long wavelengths sampling large-scale structures while short wavelengths are affected by local heterogeneities (Barth et al. 2008). Therefore, several error estimates related to the waveform recordings have to be considered for assessing the reliability and the degree of uncertainty of a focal mechanism solution. Typical measures for error include the RMS angular difference, which indicates how well constrained the nodal planes are with respect to the data, as in the case of first motion polarities for single or composite FMS (e.g. Kapetanidis 2017), DC percentage in case of a full MTS, correlation percentage or variance reduction for waveform inversion procedures, indicating the goodness of fit between synthetic and observed waveforms towards the reduction of variance in the final solution, partly depending on geometrical and signal quality constraints.

3 Stress Inversion

A remedy to the above issues towards resolving the type of faulting (Table 1) and the orientation of the principal axes of the regional stress, that is critical in seismotectonic studies, is the implementation of stress inversion. Anderson (1905, 1951) was one of the first to present a clear summary of the analysis of faults systems and vein systems by analogy with rock mechanics, providing a simple estimation of the orientation of the principal stress axes and the fault regime associated with slip directions. Wallace (1951) and Bott (1959) introduced the so-called "faultless" methods in the analysis of fault slickenside data, which were later expanded to include focal mechanisms.

Since the pioneering work of Bott (1959), several different methods for inferring certain elements of the stress tensor from populations of faults have been proposed. These can be grouped into graphical (Compton 1966; Arthaud 1969; Angelier and Mechler 1977; Aleksandrowski 1985; Lisle 1987; Marrett and Allmendinger 1990) and numerical techniques (Carey and Brunier 1974; Etchecopar et al. 1981; Armijo et al. 1982; Angelier 1984, 1989, 2002; Gephart and Forsyth 1984; Michael 1984, 1987; Reches 1987; Gephart 1988, 1990; Huang 1988; Fry 1999; Shan et al. 2004).

A variety of graphical analyses methods have been proposed for fault-slip analysis. Among these, the "P- and T-dihedra" method (Angelier and Mechler 1977) and the kinematic P- and T-axes (Marrett and Allmendinger 1990) have been proven the most robust, providing similar results with the more sophisticated numerical methods.

The inverse problem that is encountered in the numerical "faultless" methods is to reconstruct the regional stress field for given groups of observed slip vectors and fault plane orientations. The procedure identifies the principal stress directions of the local stress tensor and a factor (stress ratio) that characterizes the relative differences between the principal stresses' magnitudes. All methodologies rely on the following four hypotheses:

H_1 *Faults slip in the direction indicated by the resolved shear stress*: Seismic slip is assumed to be parallel to and in the same direction as the one indicated by the shear stress resolved on the fault plane. This is also known as the Wallace-Bott hypothesis (Wallace 1951; Bott 1959).

H_2 *The rocks are physically homogeneous*: This practically assumes that stress is uniform within the rock volume, which can usually be achieved by dividing a large study region into smaller subareas (Maury et al. 2013).

H_3 *Stress is invariant over time*: This assumption holds for paleo-stress determination, since the age of slickenside data typically cannot be specified. This limitation does not apply when using focal mechanism data, in which case it is possible to perform an analysis of the temporal variations of stress (Hardebeck and Michael 2006).

H_4 *The input focal mechanisms are independent from each other*: This is required so that the input data actually sample manifestations of slip on several faults due to a common stress regime without local stress perturbations that could have been caused by a large earthquake that occurred previously (Maury et al. 2013). This suggests that some sort of data filtering, such as declustering, might be required before the inversion takes place.

Even though the inverse techniques may be used for either fault/slickenside or earthquake focal mechanism data, the above assumptions apply more accurately to the latter (Allmendinger et al. 1989). Among the inverse methods, there are two major types of algorithms to determine the stress tensor: the **grid search** and the **least-squares** methods.

Both approaches use the minimization of the angle between the calculated shear stress and the observed slip vector as a criterion for the best fit. Their difference concerns the data regression approach. The grid search method involves a large number of regression lines, for each of which their correlation with the data distribution is calculated. The least-squares approach uses regression to directly determine the best fitting line, in terms of an equation that expresses the slope and intercept of the line that minimizes the squares of the deviations between data and model.

The inversion procedure involves a system of linear equations for a population of focal mechanisms, which can be written in a matrix form (Bott 1959):

$$A\mathbf{x} = \mathbf{y} \tag{7}$$

where A is a matrix containing nodal plane orientations, $\mathbf{y}$ is a vector containing shear stress information inferred from the rake of the focal mechanisms and $\mathbf{x}$ is the vector of unknowns related to the regional stress tensor. Since the stress field is presumed to be homogeneous (H_2), the fault location, its size and shape are unimportant. A least-squares inversion of Eq. 7 would be (Menke 1984):

$$\mathbf{x} = \left[A^{\mathrm{T}}A\right]^{-1} A^{\mathrm{T}}\mathbf{y} \tag{8}$$

The stress inversion problem is nonlinear, but can be linearized by assuming that the magnitude of the shear traction on each fault plane is approximately the same. The procedure aims at finding the stress state which minimizes the discrepancy between the resolved shear stress direction and the slip direction for all earthquakes in the data set. In practice, when only the fault orientation and the slip direction are provided by the FMS, but not the magnitude Δu of the relative displacement, only part of the regional stress tensor can be estimated regarding the direction of the principal axes and their relative magnitudes. More specifically, the inversion yields a "reduced" deviatoric stress tensor, T, characterized by four parameters, three of which define the orientations of the principal stress axes $\mathbf{S}_1, \mathbf{S}_2, \mathbf{S}_3$, and another the stress ratio (also called shape factor/ratio, stress shape, aspect ratio or stress magnitude parameter), R (Gephart and Forsyth 1984):

$$R = \frac{\sigma_2 - \sigma_1}{\sigma_3 - \sigma_1} \tag{9}$$

where σ_1, σ_2, and σ_3 are the magnitudes of the maximum, intermediate, and minimum principal stress axes of the resolved stress tensor, respectively. As R increases from 0 to 1, σ_2 decreases in the range between σ_1 and σ_3, with a value of R near 0 indicating that $\sigma_2 \approx \sigma_1$ and a value of R near 1 meaning $\sigma_2 \approx \sigma_3$ (Fig. 6). These two limits represent the cases of uniaxial extension ($R=0$) and uniaxial compression ($R = 1$), respectively, while $R = 0.5$ means that $\sigma_2 = (\sigma_1 + \sigma_3)/2$. Any combination of principal stresses which produces $R > 1$ or $R < 0$ is invalid (Gephart 1985). An equivalent parameter Φ was proposed (Angelier et al. 1982; Angelier 1984, 1989; Michael 1984, 1987):

$$\Phi = \frac{\sigma_2 - \sigma_3}{\sigma_1 - \sigma_3} \tag{10}$$

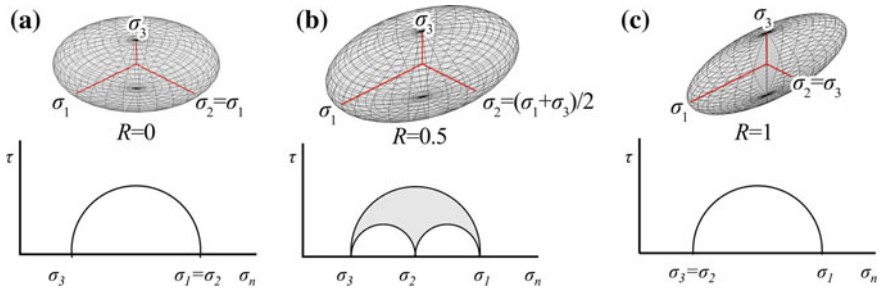

Fig. 6 Stress ellipsoids and associated Mohr diagrams for different stress states indicated by the stress ratio, R, for: **a** Uniaxial extension (R = 0, oblate ellipsoid), **b** Triaxial stress (R = 0.5), **c** uniaxial compression (R = 1, prolate ellipsoid). Note that in this example the stress magnitudes appear as all having positive values. Figure based on Lejri (2015)

The combination of (9) and (10) gives the relation $\Phi = 1 - R$. A geometrical representation of R, that is the inter-relation of the principal stress magnitudes, can be given by Lamé's stress ellipsoid and Mohr diagrams, which describe a certain state of stress (Fig. 6).

To acquire a full stress tensor, rather than a "reduced" one, further assumptions must be made about lithostatic stresses or magnitudes of shear stresses (Etchecopar et al. 1981). It is generally accepted (Byerlee 1978), that the magnitudes of shear and normal stress on the fault plane are linearly related (Amonton's Law of friction) (Eq. 2). By accepting this condition it is possible to estimate a fifth parameter, which relates the magnitudes of normal (σ_m) and shear stresses (τ_m) of the stress tensor (Allmendinger 1989):

$$\sigma_m \equiv (\sigma_1 + \sigma_3)/2 \quad \text{and} \quad \tau_m \equiv (\sigma_1 - \sigma_3)/2 \tag{11}$$

where σ_m and τ_m are the coordinate of the center of Mohr's circle and its radius, respectively (Fig. 1). A sixth parameter of the stress tensor provides a scaling factor, and thus the magnitude of all stress elements. Since this number is scaled, it cannot be estimated from orientations, which are inherently dimensionless (Allmendinger 1989). The magnitude of the displacement vector is required to estimate the scaling factor, which can be provided by surface and/or geodetic data.

Faultless methodologies are simple and fast, easy to understand and use, they have been widely implemented and provide consistent results. Despite the various conceptual differences, the most commonly used methodologies often derive comparable results for similar data sets.

3.1 Limitations of the Faultless Methods

The basic hypotheses (H_1, H_2, H_3, H_4) of the faultless methods have been questioned in cases of local and/or temporal stress perturbations; hence, one needs to verify a method's reliability on resolving the stress regime. More specifically, the main limitations of these methods are mostly attributed to: (a) the assumption that shear stress is parallel to the slip direction (H_1), (b) the assumption of stress invariance over space (H_2) and time (H_3); and an issue that can be reckoned as a limitation (c) the ambiguity of the nodal planes, which introduces an additional uncertainty when employing DC focal mechanisms instead of fault-slip data.

3.1.1 Parallelism Between Shear Stress and Slip Vector (H_1)

Faultless models do not take into account mechanical coupling of segments across the fault surface and/or mechanical interaction between adjacent fault systems, thus empirical relations are assumed to correlate slip with stress or strain. Among others, Twiss and Unruh (1998) argue on the assumption that infinitesimal strain is parallel

to shear stress caused by rotations of the finite strain. The latter may occur either due to local complications at the edges of fault blocks, or because of complex kinematic conditions at regional boundaries, invalidating inversions for stress (Gapais et al. 2000). Another parameter that can have a strong effect on the mechanical interactions on the rupture surface, hence producing heterogeneous slip vector distribution, is the friction coefficient, which affects the angle of internal friction and, consequently, the angle between fault plane and $\mathbf{S}_1$ to fulfill Coulomb's failure criterion. Reches et al. (1992) suggest the selection of an 'optimum' model among different solutions yielded by varying the friction coefficient that minimizes the sum of the angular difference between the computed regional stress tensor orientations and an 'ideal' stress tensor orientation for each dataset.

3.1.2 Stress Invariance Over Space and Time ($\mathbf{H_{2\text{-}3}}$)

The main limitations of the method come mostly from the basic hypotheses about the stress invariance both in space and time. Thus, when processes that operate at different spatial and/or temporal scales are involved, the inversion may lead to erroneous results. Any variations within the space-time window of the dataset that is considered in the faultless models are treated as noise (Angelier 1979, 1984; Angelier et al. 1982; Gephart and Forsyth 1984; Michael 1984; Reches 1987) and, hence, the validity of the inversion should be in terms of the model-data misfit. A high average misfit may indicate that the stress field is highly heterogeneous and that the stress inversion's results may not be meaningful. The problem of heterogeneous stress can be addressed by dividing the focal mechanism dataset into subsets, depending on their spatiotemporal distribution. Declustering algorithms (e.g. Wiemer 2001) can also be employed, to ensure uniform sampling over time and space or remove events below a threshold magnitude, so that the FMS used for the inversion represent ruptures caused by regional stresses rather than due to local stress perturbations.

3.1.3 Ambiguity of the Nodal Planes

A main uncertainty in defining stress using fault data is that it is impossible to identify the time of slippage. Focal mechanisms are free of this drawback (Maury et al. 2013). On the other hand, a complication of using earthquake focal mechanisms for stress inversion is that the fault plane must be distinguished between the two nodal planes, as its choice influences the derived stress tensor.

Unless a principal stress axis is parallel to the "null axis", **N**, or the considered stress tensor presents axial symmetry, with R having an extreme value, the theoretical shear stress and the slip vector cannot be aligned to both nodal planes and one of them must be chosen to represent the fault plane (Gephart 1985).

Resolving the ambiguity between the fault and auxiliary planes becomes significant when studying small variations in the stress field, since wrong selections may lead to inconclusive results and additional information should be considered, e.g.,

the distribution of seismicity, surface faulting or the kinematics of the region. The most common approach is to calculate the difference between the slip vector and the resolved shear stress orientation for both nodal planes, and choose the one that will produce the smallest misfit (Gephart and Forsyth 1984; Gephart 1990; Julien and Cornet 1987; Mercier and Gailhardis-Carey 1989). Lund and Slunga (1999) suggest the usage of an instability method based on the Mohr-Coulomb failure criterion, but only for nodal plane selection and not to be used as a misfit criterion. Others (Michael 1987; Hardebeck and Michael 2006) propose to randomly select one nodal plane when a sufficient number of focal mechanisms are available. Angelier (2002) searches for the stress tensor that maximizes the so called Shear Stress Slip Component (SSSC), τ_s, defined as the orthogonal projection of the shear stress $\boldsymbol{\tau}$ on the direction of the slip vector $\mathbf{d}$:

$$\tau_s = \boldsymbol{\tau} \cdot \mathbf{d} = \left(T\hat{\mathbf{n}}\right) \cdot \mathbf{d} \tag{12}$$

where $\hat{\mathbf{n}}$ is the unitary normal vector, T is the reduced stress tensor and $T\,\hat{\mathbf{n}}$ produces $\boldsymbol{\tau}$, the shear stress on the selected nodal plane, coplanar with the slip vector $\mathbf{d}$. The method uses grid search to find the maximum value of τ_s for k focal mechanisms:

$$S = \sum_{i=1}^{k} \tau_{s_i} \tag{13}$$

The maximum value S implies for parallelism between shear stress and slip vector (H_1), while, in addition, the magnitude of the shear stress is taken into account. Given that $\hat{\mathbf{n}_1}.\mathbf{d}_1 = \hat{\mathbf{n}_2}.\mathbf{d}_2 = 0$, by its definition, the SSSC criterion is independent of the choice between nodal planes. However, this method requires an empirical threshold on the number of minimum acceptable data to be defined (Angelier et al. 2004).

3.2 Data-Model Misfit

Validation of the acquired model is achieved through the data-model misfit. This is derived by solving the forward problem, i.e. by determining the difference between the observed slip directions and the predicted maximum shear stress directions of the model (e.g. Carey and Brunier 1974; Angelier 1984, 1984; Michael 1984, 1987). The magnitude of misfit reflects both the observational error and the degree of heterogeneity in stress orientations as determined by the focal mechanisms that have been used as input data.

Michael (1987) computes the model confidence regions by a bootstrap technique. The data set is resampled hundreds or thousands of times to simulate repeated samples of the population and each subset is inverted for the stress tensor. For a certain confidence level, a percentage of the inversion results which are closer to the preferred solution define the confidence region (Hardebeck and Hauksson 2001). Julien and

Cornet (1987) use an iterative numerical stress inversion procedure by employing the fixed point method. Hardebeck and Michael (2006) suggest a damped grid-search inversion method (SATSI), where damping is used to decrease data singularities which are treated as "random noise". Gephart and Forsyth (1984), and Gephart (1990) use a grid search, in terms of searching the best fit through a set of models, to find the best stress tensor that minimizes the misfit between model and data, suggesting equal uncertainty for fault plane orientations and slip directions. The total misfit for a given stress state is found by applying the L1- rather than the L2-norm (least absolute deviations instead of least squared ones), to avoid problems due to inconsistent or erratic data which may cause errors that do not follow a Gaussian distribution (Gephart and Forsyth 1984). With respect to Michael's (1987) method, the grid search approach yields a noticeable difference in the confidence regions only for small data sets (Hardebeck and Hauksson 2001).

Hardebeck and Hauksson (2001) by studying the stress field in southern California, using the methods of Gephart and Forsyth (1984) and Michael (1984, 1987), propose that the former provides more accurate estimates of stress orientation, especially for high-quality data sets, but the confidence regions are generally large. The method of Michael (1984, 1987) is more accurate for noisy data sets and provides a more appropriate estimate of uncertainty. Kassaras et al. (2016a), in a study of the western part of the Hellenic Arc, arrived at a similar conclusion, suggesting that the method of Michael (1984, 1987) is more suitable for investigating spatially heterogeneous regimes. Figure 7 illustrates the results from the application of the two methods in two focal mechanism datasets in Greece (Kassaras et al. 2016a) using the ZMAP software (Wiemer 2001).

The abovementioned approaches assume that all faults in the studied rock volume are activated by a uniform stress state (H_2). If that is not the case, the stress distribution is called heterogeneous. One way to handle heterogeneity is to divide the area's volume into sub-volumes and invert for stress separately for each sub-volume. However, even though this approach is frequently effective, it is characterized as subjective.

Several numerical techniques have been proposed to cope with separating stresses from spatially or temporarily varying states of stress (e.g. Yamaji 2000). Separating stresses is particularly useful in complex regimes, involving different tectonic states, which likely enhance the activation of both new and old fault systems that produce vague focal mechanisms patterns (e.g. Kassaras et al. 2014a). Moreover, the issue favorably meets the needs in the oil industry, which requires the discrimination of tectonic phases for forecasting the orientation of fractures induced by hydraulic fracturing towards ensuring drilling and borehole stability (Lejri 2015).

Most known computer programs available for the faultless method are TectonicVB (Ortner et al. 2002), FaultKin (Allmendinger et al. 2012), Faille (Etchecopar et al. 1981), FSA (Célérier 1988), Tensor (Delvaux and Sperner 2003), Stress (Michael 1984), SoftStructure (Reches 1987), Tectonics FP (Ortner et al. 2002), Tector XXI (Angelier 2002), SATSI (Hardebeck and Michael 2006), ZMAP (Wiemer 2001), MSATSI (Martínez-Garzón et al. 2014), MIM (Yamaji 2000), STRESSINVERSE (Vavryčuk 2014).

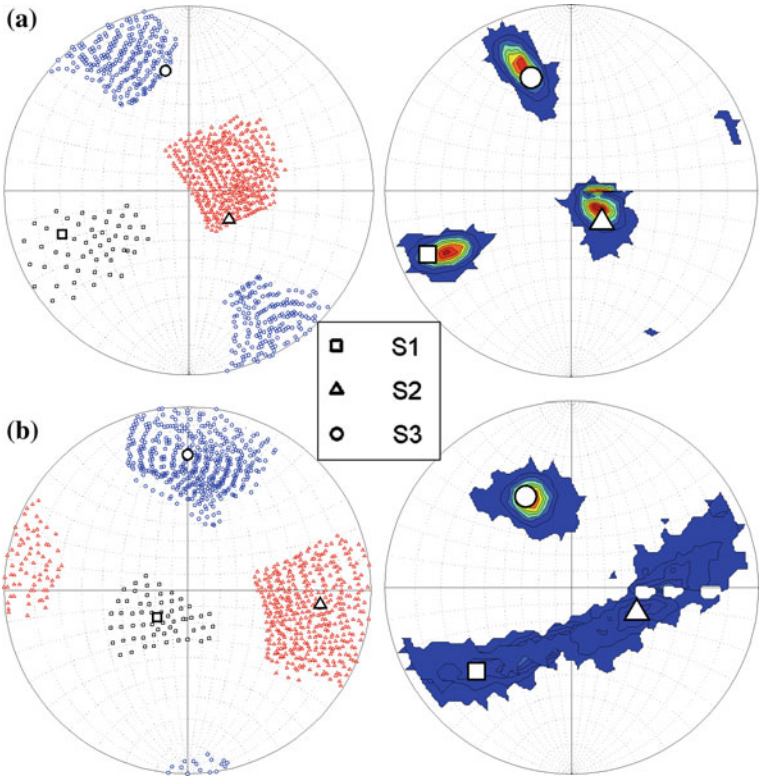

Fig. 7 Application of the methods of Gephart and Forsyth (1984) (Left) and Michael (1984) (Right) for two datasets (A, B) of focal mechanisms in W. Greece illustrating (A) similar results for both methods but larger confidence (colored regions) of the former and (B) better performance (compliant with established tectonics, Kassaras et al. 2016a) of the latter method in case heterogeneous data are involved

3.3 Geomechanical Models

The hypotheses H_1–H_3, which most of stress inversion schemes rely upon (i.e. the stress field is spatially homogeneous, temporally invariable and the direction of slip coincides with the direction of the resolved maximum shear stress), neglect the mechanical properties of the deformed region that may lead into heterogeneous slip distribution, and hence invalidate inversions for regional/remote stress (e.g. Gapais et al. 2000). Moreover, the ambiguity between the two nodal planes of the FMS introduces noise in the data when the wrong plane is selected as the fault, leading to erroneous slip vectors and interfering with the first basic assumption (H_1) (e.g. Molnar 1983; Jackson and McKenzie 1988). Another disadvantage of the abovementioned stress inversion methods concerns the data types that can be used, which are limited to fault-slip vectors and focal mechanisms.

More recently, "Geomechanical" stress inversion models have been proposed, which take into account the physical properties of the rupture surface, instead of assuming empirical relationships between slip and stress or strain (Kaven et al. 2011). The method requires knowledge of the fault geometry and information on at least one slip vector component along portions of the known fault surface(s). The concepts of fracture mechanics, such as the effects of elastic medium properties (Lamé constants), the friction and morphology of the fault surfaces and the effects of other proximal segments of the fault are considered in this method.

Both analytical (e.g. Pollard and Segall 1987; Bürgmann et al. 1994; Martel and Shacat 2006) and numerical (e.g. Segall and Pollard 1980; Maerten et al. 2005) methods have been proposed to solve the three-dimensional problem (multiple three-dimensional faults that interact mechanically) and acquire the slip distribution at every element on the fault. When displacement data are available (GPS, InSAR) the method also allows for the determination of regional stress magnitudes.

Geomechanical inversions for stress and slip distributions provide results which are comparable to principal stress axes orientations and stress magnitude ratios obtained by faultless methods (Maerten et al. 2010). Moreover, the method yields meaningful stress orientations and slip distributions when using either surface fault slickenside data, or focal mechanisms (Kaven et al. 2011). Some of the better known computer programs which have implemented the geomechanical method are Coulomb (Toda et al. 2011), based on Okada's code (Okada 1992), and Poly3D (Thomas 1993).

4 Application of Stress-Inversion on a Massive Dataset for Greece

In this section we exploit a massive dataset of individual focal mechanisms for Greece, towards investigating robustness and validity of different stress inversion methods. More specifically, our purpose is to define the degree of discrepancy/goodness of fit of each applied methodology, i.e. their consistency relative to the used FMS data and, also, in terms of interpretation, by comparing the results to quantitative strain parameters obtained by GPS measurements. Also, conclusions will be drawn on the data configuration required by each of the examined methods to reliably resolve the stress field for a given spatial scale.

The focal mechanisms dataset used is the one compiled by Kassaras et al. (2013, 2016a), which has been updated with new FMS for the purposes of the current work. The database is the outcome of thorough investigation in the literature including research papers, theses and catalogues provided by international seismological institutions. It includes 3590 individual focal mechanisms, spanning from 1861 until the end of 2016. Few focal mechanisms prior to 1962 have been derived from macroseismic observations (Papazachos and Papazachou 2003). Thereafter, the dataset follows the worldwide advances in instrumentation and computational methods. In brief, for

the period between 1962 and 1980, the era of analogue records, FMS have been determined from P-wave first motion polarities. After 1980, the beginning of the digital era, focal mechanisms of moderate and strong earthquakes were mainly obtained by moment tensor inversion using teleseismic and regional waveform modeling. A significant number of focal mechanisms in the dataset concern P-wave first motion polarities solutions for earthquakes of small magnitude ($M < 4$), recorded by temporary networks installed for the purposes of research projects (e.g. Papadimitriou et al. 1994; Hatzfeld et al. 1995; Rigo et al. 1996; Haslinger et al. 1999) or monitoring aftershock sequences (e.g. Lyon-Caen et al. 1988; Makropoulos et al. 1996; Kassaras et al. 2014a, b; Kapetanidis et al. 2015).

The dominant tectonic processes in the region (Fig. 8) include the subduction of the African lithosphere beneath the Aegean plate occurring along the Hellenic arc, the extrusion of the North Anatolian Fault (NAF) and the collision of the system with the Apulian plate and the Eurasian margin, with most of strain accommodated by the Cephalonia Transform Fault Zone (CTFZ) (Laigle et al 2002). Figure 9a presents the spatial distribution of selected focal mechanisms from the comprehensive catalogue, the vast majority of which samples the crust with an average thickness of ~35 km (Kassaras et al. 2009), while sparse events are located beneath.

By evaluating the characteristics of the focal mechanism distribution (Fig. 9) and principal stresses orientations (Figs. 10 and 11), one can ascertain that the data exhibit (a) variability, with certain areas presenting more than one type of faulting, (b) spatial sampling inhomogeneity, with some areas having more data than others, (c) significant spatial heterogeneity, implying for processes that operate at distinctly different spatial scales, with focal mechanisms of small events varying more than those of the larger ones. The inversion is expected to correctly reconstruct the stress tensor as long as the magnitude of its uniform part is larger than the one of its variable part (Michael 1991). In order for the hypotheses $H_{1\text{-}4}$ to be plausible, the data will have to be divided into subsets, mainly according to criteria concerning their spatial distribution.

Because of the sparsity of the subcrustal earthquakes, we chose to restrict the inversion within the crust by removing deep events. After removing 342 events located deeper than 35 km, the catalogue employed in the inversions is composed of 3248 individual focal mechanisms. For the presented application, the study area was divided in sub-regions of $1° \times 1°$ dimensions (Fig. 12), assuming that significant variations of the regional stress occur at a larger scale than the one chosen. This is a rather crude approximation; a better division would require the employment of seismic zones, as defined recently by state-of-the-art methodologies (e.g. Stucchi et al. 2013), but this is out of the scope of the present study, although the conclusions drawn from the analyses that follow will be useful towards this future task. Thereafter, the $1° \times 1°$ sub-regions approximation is considered feasible for the educational purposes of the current application, on the one hand, and the restrictions of our dataset to sufficiently sample the entire area of study, on the other.

The data were analyzed by implementing two numerical inversion schemes and one graphical analysis method. The graphical scheme is based on P- and T-axes analysis as it was implemented in the FaultKin algorithm of Allmendinger et al.

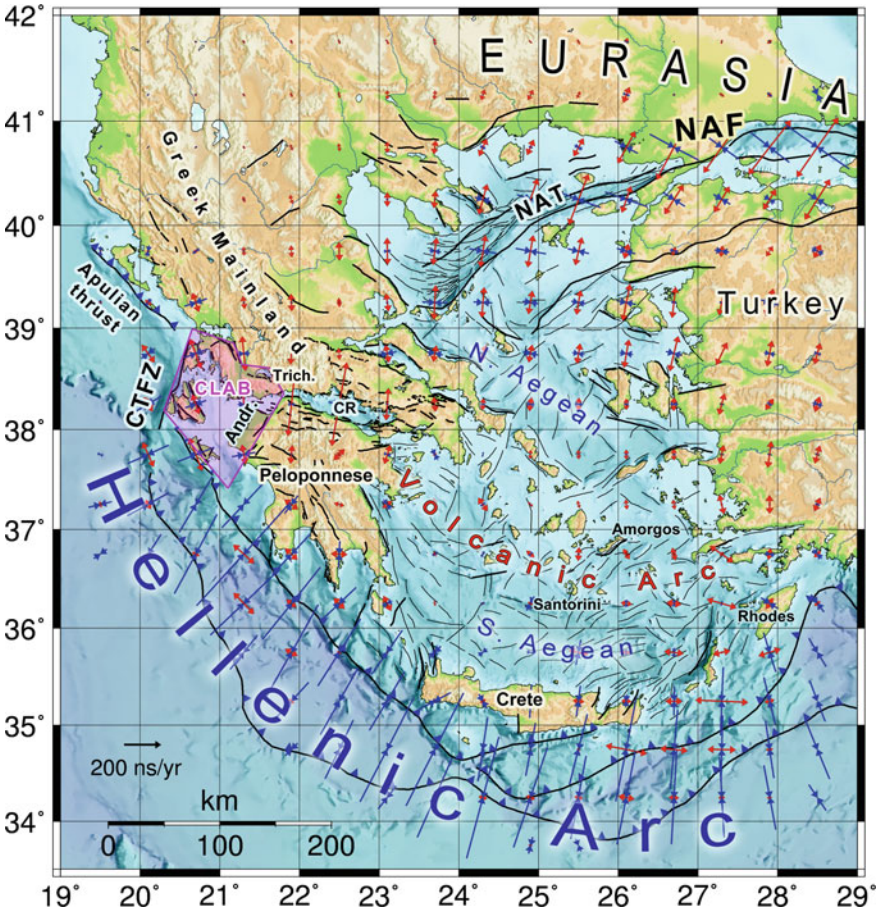

Fig. 8 Map of Greece showing the most prominent tectonic structures (Karakonstantis and Papadimitriou 2010; Sakellariou and Tsampouraki-Kraounaki 2016) and the direction of the compressional (e_{H1}-blue arrows) and extensional (e_{H3}-red arrows) principal components of horizontal strain (Kreemer et al. 2014), measured in units of nanostrain (10^{-9}) per year (ns/yr). Dextral strike-slip zones include: CTFZ: Cephalonia Transform Fault Zone, Andr.: Andravida fault, NAT: North Aegean Trough and NAF: North Anatolian Fault. Other labeled zones: CR: Corinth Rift and Trich.: Trichonis Lake while CLAB (purple polygon) marks the Cephalonia-Lefkada-Aitoloakarnania Block

(2012). The first numerical scheme is based on Michael's method (Michael 1984), using the SATSI algorithm (Hardebeck and Michael 2006) and the second one is the Multiple Inverse Method (MIM) of Yamaji (2000). Although for several regions in Greece the faulting geometry is well known, the input fault plane for the faultless methods was randomly chosen; hence a "noisy" dataset was employed aiming at investigating the resolving power of the applied methods. For the MIM, both nodal

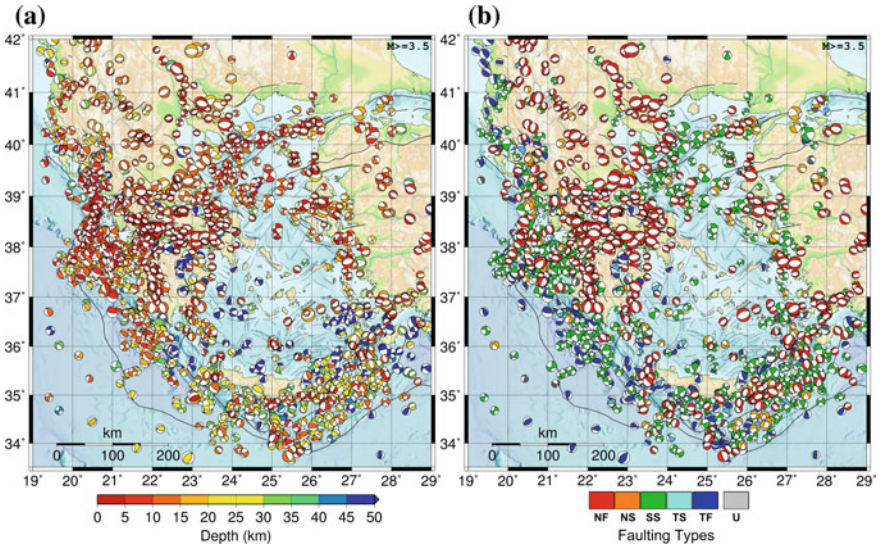

Fig. 9 Illustration of selected ($M \geq 3.5$) focal mechanism data contained in the comprehensive catalogue for Greece, **a** sorted by focal depth and **b** sorted by faulting type, according to the classification rules of Zoback (1992)

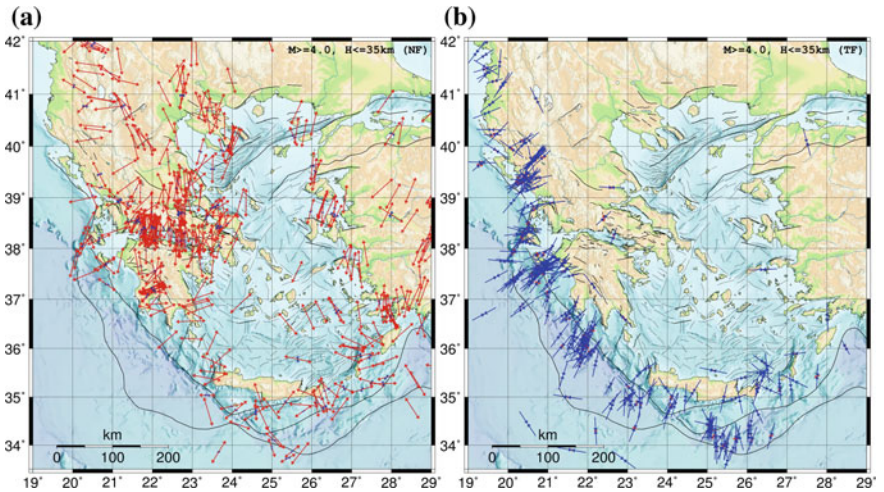

Fig. 10 Horizontal orientation of $\mathbf{S}_1$ (red) and $\mathbf{S}_3$ (blue) principal stress axes for focal mechanisms of selected ($M \geq 4.0$) crustal earthquakes ($H \leq 35$ km) in Greece, **a** for events classified as NF, **b** for events classified as TF, according to the Zoback (1992) faulting type criteria (Table 1). Vector length is proportional to the cosine of the respective axis' plunge

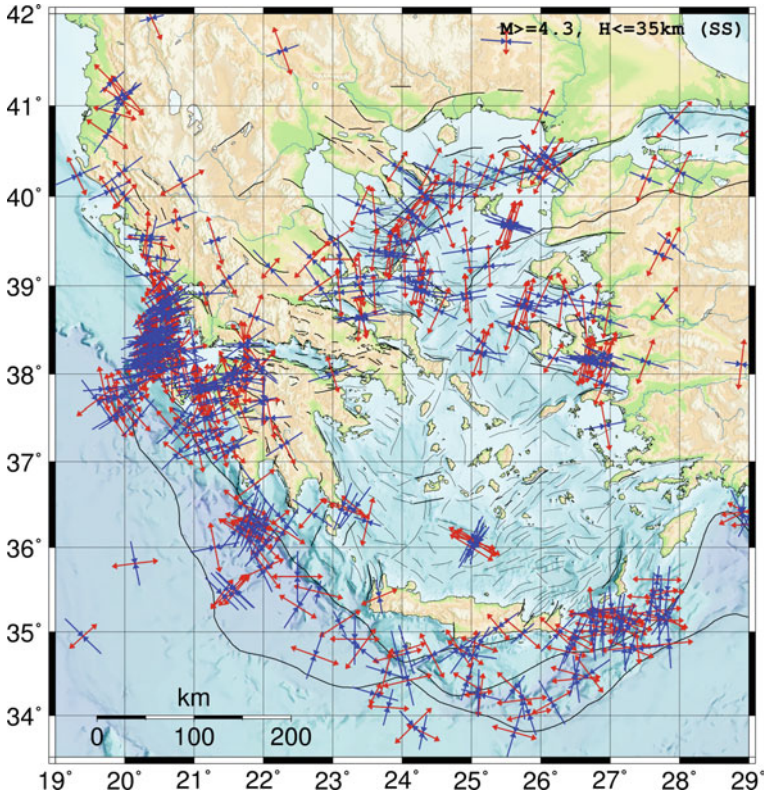

Fig. 11 Horizontal orientation of $\mathbf{S}_1$ (red) and $\mathbf{S}_3$ (blue) principal stress axes for focal mechanisms of selected ($M \geq 4.3$) crustal earthquakes ($H \leq 35$ km) in Greece classified as SS, according to the Zoback (1992) faulting type criteria (Table 1). Vector length is proportional to the cosine of the respective axis' plunge

planes were considered during resampling, excluding subsets with both nodal planes of the same focal mechanisms to avoid redundancy.

5 Results

5.1 The "FaultKin" Analysis

The methods that were described in Sect. 3 are based on the calculation of the regional stress field for given groups of observed slip vectors and fault plane orientations, which in the case of focal mechanisms are uncertain due to the nodal planes ambiguity. Besides the techniques developed for selecting the most relevant

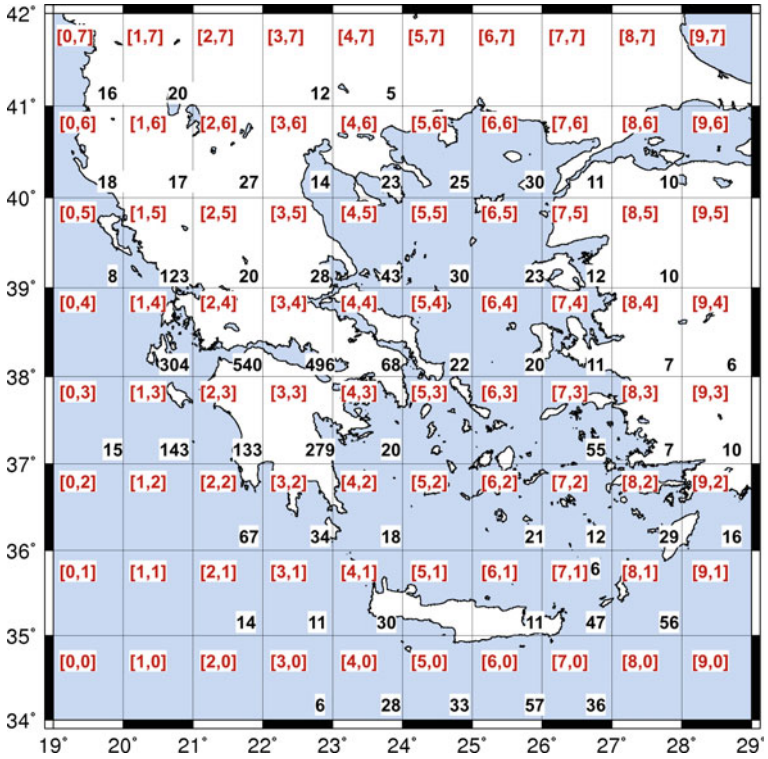

Fig. 12 The grid configuration applied for the inversions. Numbering indicates coordinates (red, upper-left) and available focal mechanisms for each sub-area (black, lower-right)

information by minimizing the data-model misfit, the degree up to which focal mechanism data are capable to reproduce the regional strain field is rather questionable. This problem arises with associating P- and T-axes either with the principal strains (Marrett and Allmendinger 1990; Twiss and Unruh 1998), or with principal stresses (e.g. Angelier and Mechler 1977; Gephart and Forsyth 1984). The concept behind the implementation of "FaultKin" analysis in our dataset is the direct association of P- and T-axes with fault geometry and sense of slip (Andersonian faulting type; Anderson 1905). Thus, the demand of defining the fault out of the two nodal planes, which is prerequisite in other methods, is eliminated.

"FaultKin", a computer program for the analysis of fault slip data (Marret and Allmendinger, 1990; Allmendinger et al. 2012), is classified among the "graphical" stress inversion methods, a variety of which has been proposed for fault slip analysis. Among these, the "P- and T-dihedra" method (Angelier and Mechler 1977) and the kinematic P- and T-axes, having been proven the most robust, seldom differing substantially from numerical analyses (Allmendinger 1989), are implemented in the Faultkin code. FaultKin uses Kamb's method (1959) for presenting orientation data, P- and T-axes are displayed as contoured plots that allow statistical

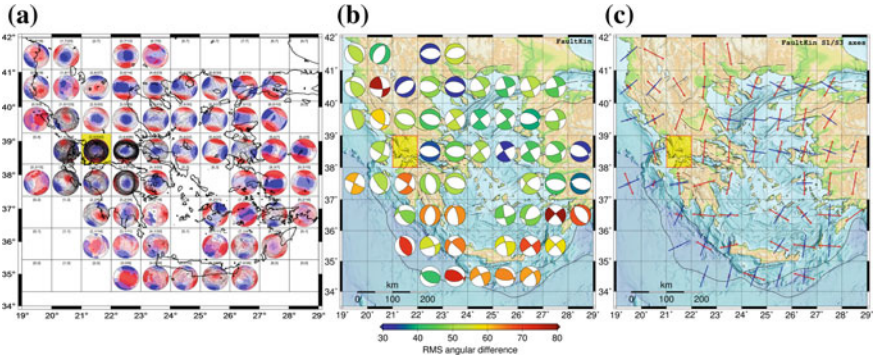

Fig. 13 Maps illustrating the results of the FaultKin inversion: **a** Stereo plots show contouring of **P**- (blue) and **T**-axes (red) of the focal mechanism subsets using Kamb's (1959) method, **b** unweighted summed moment tensor per sub-region (Eq. 14) with respect to the RMS angular difference between the individual input focal mechanisms dataset and the obtained solution for each cell, and **c** the arrangement of the projections on the horizontal plane of the resolved best-fit principal stress components $\mathbf{S}_1$ (blue) and $\mathbf{S}_3$ (red) for the combined moment tensors per sub-region. The yellow cell at [2, 4] denotes an unresolved stress tensor due to the high heterogeneity of the focal mechanisms dataset (Fig. 14)

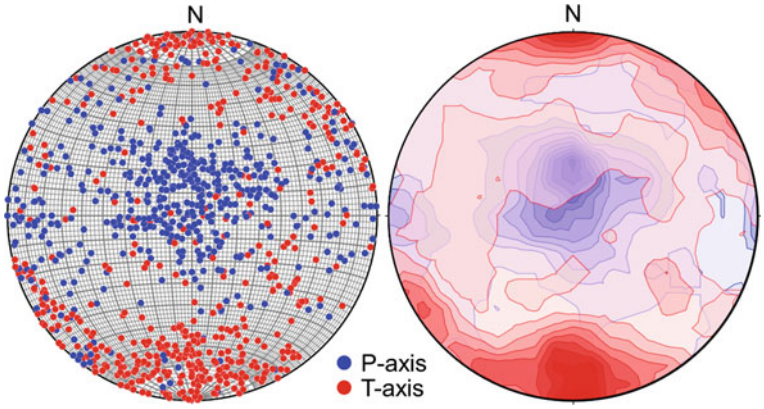

Fig. 14 Stereoplots produced by FaultKin, indicating the heterogeneous distribution of the input focal mechanisms P- and T-axes in the NE part of the CLAB (grid [2, 4] in Fig. 12; see also Figs. 8 and 13a): **a** scatter plot, **b** contour plot (Kamb 1959)

inferences to be drawn directly from the stereonet diagrams (Figs. 13a and 14b). An unweighted moment tensor summation scheme is used by applying the Bingham distribution (Binham, 1964; 1974), which can successfully describe circular, elliptical or bar/axes distributions and has been often used for delineating structural orientations (e.g. Yamaji 2016). The unweighted moment tensor is composed of the sums of the products and the squares of the direction cosines of the individual P- and T-axes (Allmendinger 1989):

$$M = \begin{vmatrix} \sum(\mathrm{CN(P)})^2 - (\mathrm{CN(T)})^2 & \sum \mathrm{CN(P)} * \mathrm{CE(P)} - \mathrm{CN(T)} * \mathrm{CE(T)} & \sum \mathrm{CN(P)} * \mathrm{CD(P)} - \mathrm{CN(T)} * \mathrm{CD(T)} \\ \sum \mathrm{CE(P)} * \mathrm{CN(P)} - \mathrm{CE(T)} * \mathrm{CN(T)} & \sum(\mathrm{CE(P)})^2 - (\mathrm{CE(T)})^2 & \sum \mathrm{CE(P)} * \mathrm{CD(P)} - \mathrm{CE(T)} * \mathrm{CD(T)} \\ \sum \mathrm{CD(P)} * \mathrm{CN(P)} - \mathrm{CD(T)} * \mathrm{CN(T)} & \sum \mathrm{CD(P)} * \mathrm{CE(P)} - \mathrm{CD(T)} * \mathrm{CE(T)} & \sum(\mathrm{CD(P)})^2 - (\mathrm{CD(T)})^2 \end{vmatrix} \quad (14)$$

where CN, CE, CD denote the North, East and Down direction cosines (NED) of the P- and T-axes, respectively. The eigenvalues and eigenvectors of M give the relative magnitudes and orientations of the three kinematic axes $\mathbf{S}_1$, $\mathbf{S}_2$, $\mathbf{S}_3$, respectively. A detailed description of the theoretical background of the method can be found in Marrett and Allmendinger (1990), and Allmendinger et al. (2012).

A user-friendly interface is provided by the "FaultKin" software, while data and results are displayed as graphical plots. The input from individual focal mechanisms includes strike, dip and rake of one nodal plane, following the Aki and Richards (2002) convention. In this format, with the slip vector representing the relative displacement of the hanging wall with respect to the footwall, the rake is measured counterclockwise from the strike direction to the slip vector, so that faults with a thrust component have a positive rake and those with a normal component have a negative rake. Equal uncertainty is assumed for fault plane orientations and slip directions. The output is the orientation (trend) and dipping (plunge) angles of the three principal axes of the stress tensor, the faulting parameters (strike, dip, rake). Details on the program's usage and its capabilities can be found in Allmendinger (2016).

Application of the Method

For each dataset corresponding to a sub-region of $1° \times 1°$ dimensions, the kinematic P- and T-axes analysis was applied. The results of the FaultKin procedure are presented in Fig. 13. Contoured plots in Fig. 13a indicate large heterogeneity for the majority of sub-regions, especially in the NE area of the CLAB (Fig. 8), where the reduced stress tensor could not be resolved by the method (rectangle with yellow fill in Fig. 13a, cell [2, 4] in Fig. 12). The heterogeneity of strain release in this area is evidenced by the scatter and Kamb plots of Fig. 14. The results are generally in close accordance to the expected stresses from the breakdown of data to different faulting types (Figs. 10 and 11).

The misfit between the optimal stress tensor, as derived by the inversion, and the individual FMS input data is measured in terms of the RMS angular difference between the optimal $\mathbf{S}_1$, $\mathbf{S}_2$, $\mathbf{S}_3$ and the respective orientations of the FMS eigenvectors **P**, **N**, **T**. The angular difference, $\delta\theta$, between two tensors with normalized eigenvectors represented by matrices **A** and **B**, respectively, is defined as the minimum angle of rotation, also known as "Kagan angle" (Kagan 1991; Tape and Tape 2012), that must be applied relative to a special axis so that the rotated **A** becomes equal to **B** (Kapetanidis 2017). The optimal 3D rotation matrix, **R**, is calculated using a method called "Kabsch algorithm", which provides the transformation that minimizes the RMS deviation between two sets of vectors in their exact order (Kabsch 1978). The rotation matrix, **R**, can then be converted to an axis/angle representation by a procedure known in the literature as the inverse of Rodrigues' rotation formula (e.g. Shuster 1993). The procedure has to be repeated for all combinations with each

of the eigenvectors pointing to either direction, e.g. $\mathbf{S}_1$ and $-\mathbf{S}_1$, in order to find the minimum angle $\delta\theta$ between **A** and **B**.

5.2 The SATSI Stress Inversion

Faultless methods rely on the assumption of stress uniformity within space and time (H_2–H_3). Accordingly, inversions are conducted within volumes of a small enough size for the assumption of stress uniformity to remain valid (Plateaux et al. 2010). The fit of a stress tensor is performed independently to the focal mechanisms of each sub-area, regardless of noisy or non-uniquely fitting data that does not completely constrain the stress tensor (Hardebeck and Michael 2006).

SATSI (Spatial And Temporal Stress Inversion, Hardebeck and Michael 2006) is a modified version of Michael's code that inverts focal mechanism data for a spatially and/or temporally varying stress field. The stress field in SATSI is resolved by dividing a region into sub-regions and inverting the focal mechanisms simultaneously for all sub-regions, searching for the optimal stress within each cell while minimizing the stress differences between neighboring regions (Hardebeck and Michael 2006). Hence, apart from the noisy data issue, it also smoothens out anomalous stress perturbations that may be unimportant for the regional stress state configuration.

A damped grid-search is used in the method to optimize the fit between the observed and the calculated stress parameters by minimizing the weighted sum of two values: the data misfit and the model length. The model length is represented by the L2 norm of the vector containing the differences between each stress tensor component for each pair of adjacent grid points. The damped inversion helps in removing stress artifacts exhibited by isolated data singularities and resolving sharper true stress rotations compared to a simple smoothed model or a moving-window inversion (Hardebeck and Michael 2006).

Since appropriate damping should produce a regional stress field model that contains only those variations of the stress field that are strongly related to the data (Hardebeck and Michael 2006), in the first stage of the procedure, the optimum damping parameter, e, is searched. This parameter controls the amplitude of the solutions' variations between neighboring sub-regions. It is usually chosen from a range of damping values using the trade-off curve between the data misfit and the model length (e.g. Eberhart-Phillips 1986) to produce a balance between excessive misfit and unnecessary model length (Hardebeck and Michael 2006). In the second step, the stress inversion is performed and the best stress tensors are found for each grid point. Finally, the input dataset is resampled using a bootstrap procedure and the confidence intervals of the stress tensor axes are computed. The uncertainty for each grid node is determined as the range of stress orientations for this set of models (Hardebeck and Michael 2006).

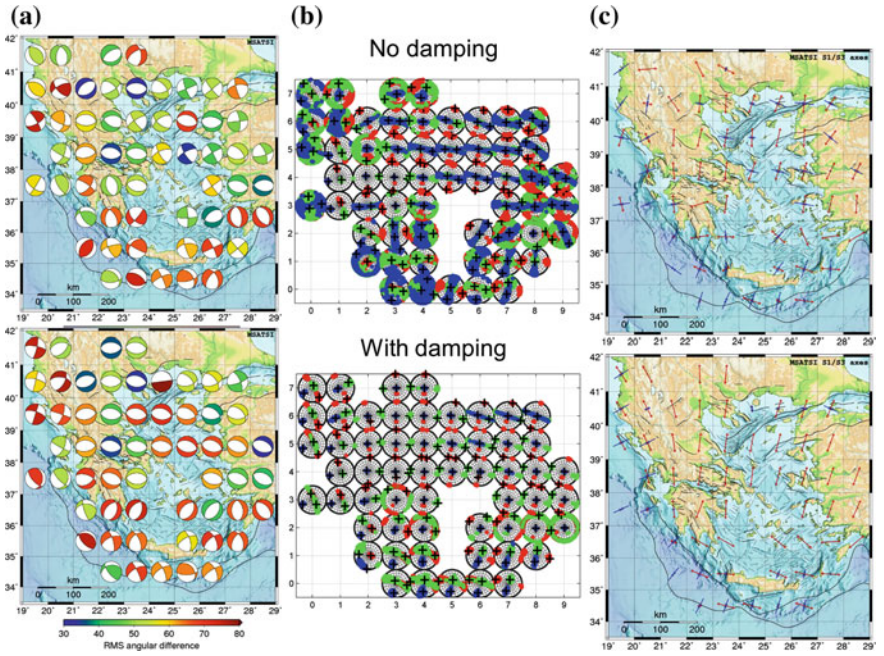

Fig. 15 Maps illustrating the results of the MSATSI inversion for 57 sub-regions. (Top) without damping; (Bottom) with auto damping ($e=2$); **a** the inverted focal mechanisms with respect to the RMS angular difference between the focal mechanism dataset and the obtained solution for each grid point. **b** Stereo plots showing the 95% confidence regions of 2000 bootstrap resamples for the $\mathbf{S}_1$ (blue), $\mathbf{S}_2$ (green) and $\mathbf{S}_3$ (red) axes, and **c** the arrangement of the projections on the horizontal plane of the resolved best-fit principal stress components $\mathbf{S}_1$ (blue) and $\mathbf{S}_3$ (red)

Application of the Method

We applied the SATSI method using the MSATSI software (Martínez-Garzón et al. 2014). MSATSI facilitates an automated procedure and MATLAB based visualization tools to represent the inversion results using a variety of plots. The inversion of the individual focal mechanisms for the subset of 3248 shallow events was performed over the $1° \times 1°$ grid of Fig. 12, using at least 5 focal mechanisms for each rectangle, by adopting solutions lying within the 95% confidence interval of 2000 resamples as determined by the bootstrapping method (Hardebeck and Michael 2006). For comparison, the SATSI inversion was performed with and without damping (Fig. 15). In the first case, the damping parameter was determined at $e=2$ by the aforementioned 'knee' of the trade-off curve between the data misfit and the model length.

The RMS angular difference between the input FMS datasets and the respective stress tensor's orientation, as obtained for each sub-region (Fig. 15a), appears relatively high, likely related to the ambiguity of the input nodal planes and the heterogeneity of the data. Considering the un-damped/damped solutions, the former exhibits smaller RMS angular difference values and broader confidence regions for

the geometry of the principal stress axes (Fig. 15b), typically observed in sub-regions with sparse sampling of focal mechanisms or in cases of high heterogeneity, as in the NE part of the CLAB (Fig. 14).

5.3 The Multiple Inverse Method (MIM)

A broadly implemented method aiming to separate stresses from heterogeneous fault slickenside data and later on from focal mechanism data is the Multiple Inverse Method (MIM) of Yamaji (2000), which employs a resampling technique (Otsubo and Yamaji 2006; Otsubo et al. 2008; Yamaji and Sato 2011). It utilizes the Hough transform, an image processing method based on hierarchical clustering (e.g. Leavers 1992). In this scheme, the fitness of a stress state to a fault-slip/focal mechanism datum is evaluated using the angular misfit, d, between the observed and theoretical slip directions. A symmetric function, $\rho(d)$, of arbitrary form (e.g. $\rho(d) = (\cos|d| + 1)/2$), with a unique maximum at $d = 0$, is used as a fitness criterion (Choi et al. 1996; Yamaji et al. 2006). The procedure samples repeatedly k-fault subsets from a given set of data and calculates the optimal stress for each subset by applying iteratively the Angelier's (1979) inversion scheme. The optimal stress for each sample subset is determined by maximizing a function called "M-estimator" (Yamaji et al. 2006; similar to Eq. 14):

$$M(\sigma) = \frac{1}{\mathrm{N}} \sum_{k=1}^{N} \rho(d(k, \sigma)) \tag{15}$$

where N is the number of fault-slip (or FMS nodal planes assumed as fault planes) in the subset and $d(k, \sigma)$ is the misfit angle of the kth fault datum for the respective trial tensor, σ. $M(\sigma)$ presents a peak when σ is compatible with one or more subsets. Namely, the match of each datum to various reduced tensors is represented by a spike in $M(\sigma)$; thereafter, significant stresses are separable according to the prominent peaks of $M(\sigma)$. Each kth point is projected on the surface of a unit hypersphere in a five-dimensional Euclidean space, representing five parameters that define the reduced stress tensor (orientation of $\mathbf{S}_1, \mathbf{S}_2, \mathbf{S}_3$, stress-ratio R or Φ) and the fault-slip generated through the application of hypothesis H_1 (Otsubo et al. 2006). Individual observations are plotted as tadpole symbols (5-elements reduced stress tensors) on the 5D hypersphere (i.e. panels b and c in Fig. 16). Distinct stress states compatible with a dataset are identified as groups of reduced stress tensors on the hypersphere (similar characteristics) by k-means clustering. The latter method needs a well-defined distance parameter to quantify the uncertainty of the resolved stresses. The required metric is provided by the great-circle distance between points on the hypersphere, termed "angular stress distance", Θ; the optimum partitioning into clusters (stress states) is determined by minimizing the sum of squared distances (stress angles) between each point and the respective cluster's center, also referred to as "spread"

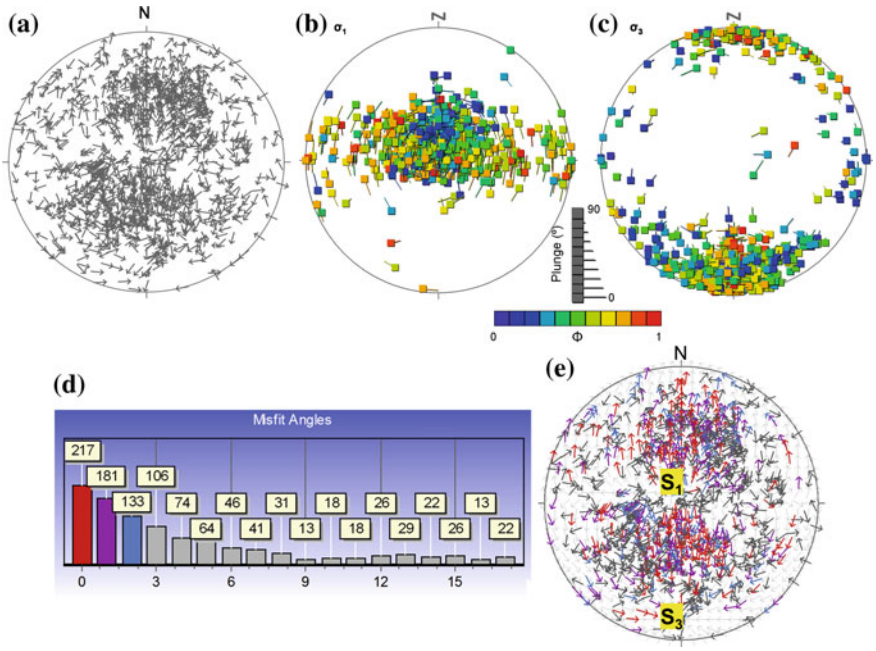

Fig. 16 Stereograms presenting the projection of: **a** tangent-lineation diagram of the input data without filtering, **b**, **c** optimized diagrams of tadpole symbols for (**b**) σ_1 ($\mathbf{S}_1$) and (**c**) σ_3 ($\mathbf{S}_3$) after declustering (Screening #1) and removal of erroneous data by using the EF option (Screening #2). The $\mathbf{S}_1$ tadpole tails indicate the azimuth and plunge of the corresponding $\mathbf{S}_3$ vector and vice versa for the $\mathbf{S}_3$ tail. **d** Histogram presenting the data-model misfit angles in terms of the slip vector orientations. The horizontal axis is in tens of degrees. The vertical axis denotes the multitude of reduced stress tensor pairs with the corresponding misfit value. **e** Diagram showing tangential-lineation of the input data, color-coded with respect to the misfit angles shown in panel (**d**). Thin gray arrows denote fault movements predicted by the Wallace-Bott hypothesis for the resolved stress state

(Otsubo et al. 2008). Significant stresses in the FMS dataset can be identified graphically as concentrations of tadpoles with similar colour, tail direction and length (see Fig. 16).

The MIM considers both the nodal planes of DC focal mechanisms during the resampling procedure to account for the fault/auxiliary plane ambiguity. The resolution can be improved by discarding subsets which contain both nodal planes of the same focal mechanism (the data need to be independent) or those not compatible with any single state of stress. The latter is considered when the theoretical slip direction makes a sufficiently large angle with the observed one; a subset is left out if no tensor is compatible with any of its members (Otsubo and Yamaji 2006; Otsubo et al. 2008).

The identification of significant stresses and the grouping of faults follow the classical scheme of Wallace-Bott, that is to minimize the sum of misfit angles

(d_T) between observed and calculated slip directions. Threshold values in the range $15° \leq d_T \leq 30°$ are suggested, with the 20° being the most preferable (Yamaji and Sato 2011).

Application of MIM

This section presents the application of MIM to selected sub-regions ($1° \times 1°$ cells; Fig. 12) that exhibit a particularly high degree of heterogeneity. An integer in the range $2 \leq k \leq 8$, called "data combination number" (Yamaji and Sato 2011), is allowed in the inversion, whilst for focal mechanism data $k = 5$ is suggested (Yamaji et al. 2011). However, due to performance restraints of the code, a limitation exists regarding the number of iterations, which depends on the multitude N of the dataset (maximum $N = 96$ focal mechanisms are allowed in the current 32-bits version of the code). If larger datasets are employed, a reduction of k is required. Since our datasets exceeded in several cases the allowed dimensions, the choice of k was decided accordingly between the values of 3 and 5.

A detailed description of the implementation of the procedure can be found in Yamaji et al. (2011). Hereby, we present the most important steps followed for the MIM analysis of the Greek dataset, namely for (a) the [2, 4] sub-area (Fig. 12) at the NE part of the CLAB (Fig. 8), for which the Faultkin scheme failed to provide any solution due to the high heterogeneity of the involved data (Figs. 13a and 14), and (b) the [5, 5] sub-area related with NAT (Fig. 8) for which FaultKin and undamped SATSI solutions provided controversial results compared to the damped SATSI solution (Figs. 13 and 15).

Sub-region [2, 4]—NE part of the CLAB

This area is characterized by complex tectonics related to different types of faulting, possibly acting at different scales (Kassaras et al. 2014a). More specifically, it contains (a) NNW–SSE structures parallel to the modern Hellenic Arc (McKenzie 1972; LePichon and Angelier 1979) and following the geometry of the fold-and-thrust belt of the External Hellenides (e.g. Philippson 1998), (b) Holocene ~E-W trending normal faults (Kapetanidis 2017) developed on top of the thrust sheets of the Hellenides (Mariolakos and Papanikolaou 1987) and (c) NE-SW dextral strike-slip structures, parallel to the CTFZ, suggested to be related to the Central Hellenic Shear Zone (Papanikolaou et al. 2009) and the North Anatolian Fault Zone (Serpetsidaki et al. 2014).

Figure 16 presents the stress field resolved for each k set of data produced by continuous resampling of the focal mechanisms dataset. The diagrams of Fig. 16b, c are the result of an optimization procedure of the MIM including: (a) the removal of subsets with obsolete nodal planes that correspond to similar focal mechanisms and do not contribute to the solution (termed Screening #1 in MIM; Otsubo et al. 2008), which has a similar effect to the declustering of aftershock sequences, thus fulfilling the assumption H_4, (b) rejection of subsets with a spread that surpasses the misfit threshold ($d_T = 20°$) for any possible stress configuration (termed Screening #2 in MIM; Otsubo et al. 2008), and (c) a procedure that employs a user-defined "enhance factor" (EF), combined with the kth stresses standard deviation with respect to the

Table 2 The average stress state resolved for cell [2, 4]

Node	Lat (°N)	Lon (°E)	Stress state A				
			S_1 (°)		S_3 (°)		Φ
			Trend	Plunge	Trend	Plunge	
[2, 4]	38.5	21.5	352	77	183	12	0.5

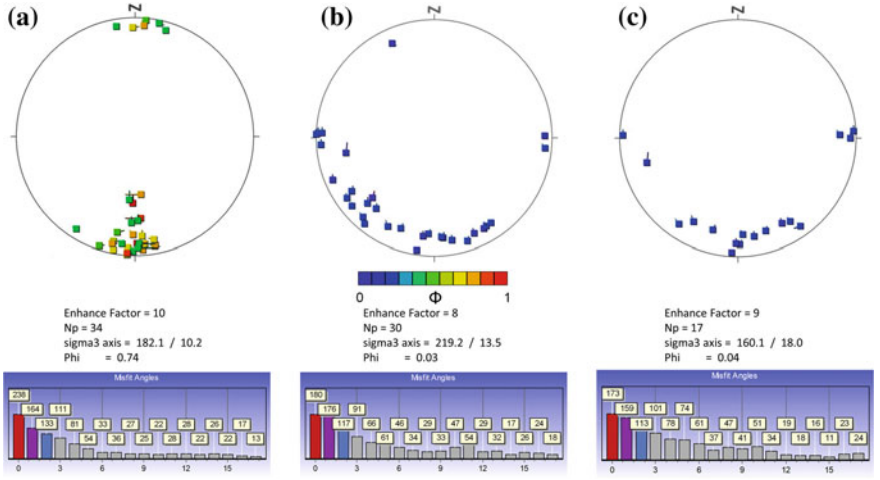

Fig. 17 (Top panels) Stereograms presenting the $\mathbf{S}_3$ stress axes distribution of k-subsets across the hypersphere. "Filtering" of k-means data points is based on the aforementioned optimization procedure with: **a** EF = 10, Φ = 0.74, **b** EF = 8, Φ = 0.03 and **c** EF = 9, Φ = 0.04. Np is the number of tadpole symbols (reduced stress tensors) plotted on each stereogram. Bottom panels present the distribution of the respective angular misfit between the calculated and observed slip directions. The horizontal axes are in tens of degrees. The vertical axes denote the multitude of k-means solutions for each bin

global solution, to thin out erroneous solutions and enhance correct ones (Yamaji 2000). Although a complicated pattern is derived in terms of the stress shape (Φ), the filtered distribution of individual reduced stress tensors (Fig. 16b, c), is more indicative of a physical process (i.e. a distinct stress state) than the initial noisy distribution of the tangential slip on the nodal planes (Fig. 16a).

The average stress state resolved by the MIM (Table 2) implies for sub-vertical $\mathbf{S}_1$ and sub-horizontal (approximately N-S) $\mathbf{S}_3$, compatible with normal E-W faulting in the area. The obtained pattern is very similar to the one obtained by the SATSI procedure for this sub-region (Fig. 15). However, stress is highly variable as the data-model misfit angles distribution shows (Fig. 16d, e), consistently with Kassaras et al. (2012), who found predominant extension axes at different directions throughout this area. Indeed, by using different EFs and by applying selection of stresses according to Φ values, it has been made possible to distinguish between different $\mathbf{S}_3$ orientations, found to range between ~N160° and ~N220° in the region (Fig. 17).

The histograms in Fig. 17, presenting the misfit angles between the inverted and the observed slip directions, indicate that an $\mathbf{S_3}$ orientation of ~N180° explains well the majority of the observations. The ~N220° and ~N160° $\mathbf{S_3}$ arrangements, appear compatible with a smaller number of tadpole symbols, which present large dispersion across the hypersphere (blue tadpoles in Fig. 17), likely related to the large heterogeneity of the input dataset.

Sub-region [5, 5]—North Aegean

The MIM analysis was applied (for sub-area [5, 5], Fig. 12) in north Aegean, where damped SATSI yielded ~NS extension, compatible with EW normal faulting, whereas FaultKin and un-damped SATSI yielded almost horizontal $\mathbf{S_1}$ and $\mathbf{S_3}$ axes, corresponding to strike-slip style of faulting. The latter is consistent with the prominent branches of the dextral strike-slip North Anatolian Fault (NAF) in the area (Fig. 8). Figure 18 presents the distribution of k-FMS resampling inversion solutions as tadpole symbols, color coded according to the value of the shape ratio (Φ), while Table 3 summarizes the outcome. The results of the analysis exhibit two distinct stress clusters A and B, with different positions within the hypersphere separated by an angular stress distance $\Theta = 57°$ and also different Φ values. Small data-model misfit angles (Fig. 18) indicate that both stress states have been efficiently resolved. Stress state A infers strike-slip faulting, compatible with right-lateral motion when a NE-SW nodal plane is considered as the fault plane, in agreement with the expected tectonic regime in the westwards continuation of NAF. Stress state B implies for N-S extension on ~E-W conjugate faults, compatible with the orientation of pull-apart basins in north Aegean, i.e. extensional basins at the tips of conjugate strike-slip faults (e.g. Ganas et al. 2005). As a conclusion, the obtained results indicate an efficient performance of the MIM scheme on resolving patterns where more than one stress states are distinctly involved.

6 Discussion—Conclusions

In this work we overview state-of-the-art stress inversion methodologies using earthquake focal mechanism data. We have applied three methods based on the Wallace-Bott "faultless" approximation for determining the regional stress in Greece by employing a comprehensive focal mechanisms dataset (Kassaras et al. 2016a). The regional stress field was determined in terms of the reduced stress tensor that includes the orientations of the principal stress axes $\mathbf{S_1}$, $\mathbf{S_2}$, $\mathbf{S_3}$ and the shape ratio (R or Φ). The inversion schemes applied are: FaultKin (Allmendinger et al. 2012), SATSI (Hardebeck and Michael 2006), and MIM (Yamaji 2000). FaultKin belongs to the graphical methods for P- and T-axes analysis, SATSI applies the Michael's (1984) method combined with spatial and temporal smoothing and MIM (Yamaji 2000) applies Angelier's (1979) technique and hierarchical clustering (Leavers 1992).

In general, the three methods provided comparable results in most regions regarding the eigenvectors of the principal stress axes $\mathbf{S_1}$, $\mathbf{S_2}$, $\mathbf{S_3}$. However, the resolving

Table 3 The two stress states resolved for cell [5, 5] in north Aegean. Θ denotes the angular stress distance between the two stress states, A and B, on the hypersphere

Node	Lat (°N)	Lon (°E)	Stress state A					Stress state B					Θ (°)
			S_1 (°)		S_3 (°)		Φ	S_1 (°)		S_3 (°)		Φ	
			Trend	Plunge	Trend	Plunge		Trend	Plunge	Trend	Plunge		
[5, 5]	39.5	24.5	277	9	9	12	0.5	243	90	7	0	0.75	57

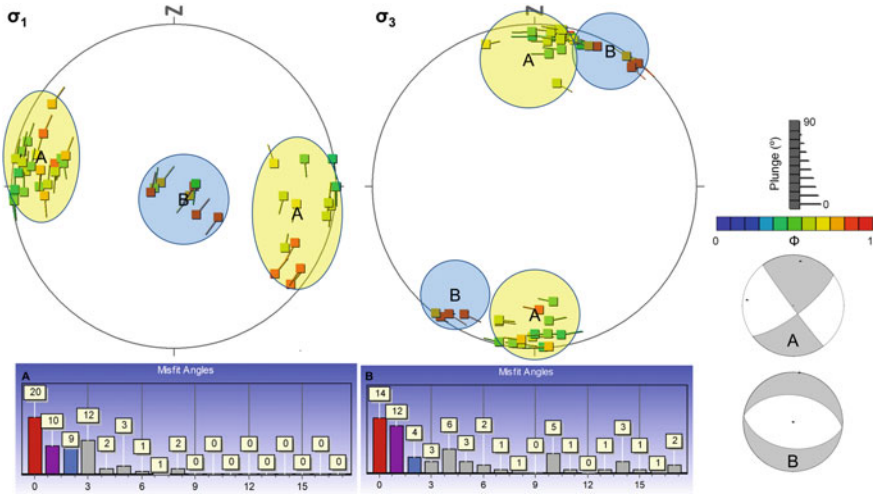

Fig. 18 Stereograms presenting the projection of $\mathbf{S}_1$ and $\mathbf{S}_3$ (with corresponding magnitudes σ_1, and σ_3). The notation is similar to Fig. 16. Colored areas indicate k-means clusters characterized as stress states A (yellow) and B (blue). The beachballs (bottom-right) correspond to the Andersonian (Anderson 1905) faulting types that can be produced by stress states A and B (assuming $\mathbf{P} \equiv \mathbf{S}_1$ and $\mathbf{T} \equiv \mathbf{S}_3$). Bottom panels present the data-model misfit angles for the two stress states (A, B). The horizontal axes are in tens of degrees. The vertical axes denote the multitude of k-means solutions for each bin

power of the different methods was found to vary. FaultKin resolved 56 out of 57 datasets corresponding to $1° \times 1°$ sub-regions, failing to invert cell [2, 4], a largely heterogeneous dataset at the NE part of the complex CLAB area (Fig. 8). SATSI provided results for all the sets of data. The un-damped SATSI procedure yielded similar results with those of FaultKin, but also managed to resolve cell [2, 4]. Both models exhibit quite large uncertainties for tectonically complex and sparsely sampled sub-regions. Damped SATSI yielded a consistent, smoothly varying model; however discrepancy occurs compared to the un-damped SATSI and FaultKin solutions, especially for the north Aegean (NAT). Judging by the resolved strain field (Fig. 8) and the distribution of **P** and **T** axes for individual FMS of different faulting types (Figs. 10 and 11), we suggest this discrepancy to be the effect of over-smoothing of the damped model that leads into artifacts for this region by treating real stress perturbations as "noise". In this respect, damping improves the model by smoothing only over adjacent regions where an individual stress tensor is efficiently resolved and where there is lack of strong contrast in the stresses. Otherwise, when the stress field is expected to exhibit strong variations, sub-regions should be further subdivided, likely including some degree of overlapping between neighboring cells, or more appropriate techniques for resolving heterogeneous datasets should be employed.

MIM, a technique suggested to sufficiently resolve heterogeneous stresses, was applied for the two datasets (NE part of CLAB and NAT), for which SATSI and FaultKin failed due to the aforementioned issues. Thanks to a sophisticated proce-

dure, including redundant/erroneous data removal, hierarchical stress clustering and Φ filtering, MIM enabled the distinction of different stress states within each dataset, consistent with known active tectonics in both sub-regions.

The outcome of the FaultKin and un-damped/damped SATSI inversions shown in Figs. 13 and 15 infers for predominant extensional and strike-slip tectonics. Extensional tectonics, resolved by both inversion schemes, is widely observed across the continental part of the Greek territory. Along CTFZ and the Hellenic Arc mainly strike-slip tectonics with a reverse component is observed. Reverse faulting has been resolved only in NW Greece and offshore west/south Peloponnese and Crete, with the principal axis of compression being perpendicular to the Hellenic Arc (clearly observed from the axes of individual focal mechanisms in Fig. 10b). These results are in good agreement with Kassaras et al. (2016a) and Konstantinou et al. (2017), demonstrating that the applied methods succeeded, in general, to provide a meaningful stress state in this area.

The region of CLAB is well known for complex deformation (e.g. Chousianitis et al. 2015; Perouse et al. 2016), as it is situated between the Apulia-NW Greece continental collision and the Hellenic oceanic subduction and is possibly related to a large scale shear zone which bridges NAT with CTFZ (e.g. Royden and Papanikolaou 2011). Despite the data heterogeneity, SATSI inversions resolved a ~N-S extensional regime, compatible with regional kinematics (e.g. Chousianitis et al. 2015). The application of MIM in this area highlights distinctly variable orientations of the $\mathbf{S_3}$ stress axes between ~N160°–220°. Similar results were obtained by Kassaras et al. (2012). This is likely the effect of conjugate planes' interaction producing all types of faulting (Kassaras et al. 2014a).

To the east, the FaultKin and the un-damped SATSI inversions converge into strike-slip tectonics, related to dextral motion in north Aegean (NAT) and sinistral motion in the south Aegean and in the troughs south of Crete and Rhodes islands (Sakellariou and Tsampouraki-Kraounaki 2016). In the area of NAT though, FaultKin resolved prevailing maximum horizontal compression in ~E-W direction and N-S extension (producing SW-NE trending, dextral strike-slip faulting), while un-damped SATSI indicates a less pronounced horizontal E-W compression, with dominant N-S extension in some cells. For the same region, the damped SATSI inversions yielded pure N-S extension, which is considered as an artifact due to lateral over-smoothing of the model. This effect is likely connected with the heterogeneity of the input data, as measured by the RMS angular differences in Figs. 13 and 15. Nonetheless, the regime in the area of NAT is not straightforward and further analysis is required, since the application of MIM highlights two distinct stress states capable for producing strike-slip and normal faulting, attributed to the dextral motion of NAT and tensile motion between conjugate strike-slip faults (e.g. Ganas et al. 2005), respectively. Eastwards, in continental Turkey, all methods converge in ~N-S extensional tectonics, similar to what is observed in continental Greece north of Peloponnese (Figs. 13 and 15).

In addition, towards evaluating the outcome, we compare the resolved stress field to qualitative displacement data as represented by the strain-field (Fig. 8). Figure 19, presents the minimum 3D misfit angle, or "Kagan angle" (Kagan 1991; Tape and Tape 2012), between the resolved stress tensor and the respective strain tensor available

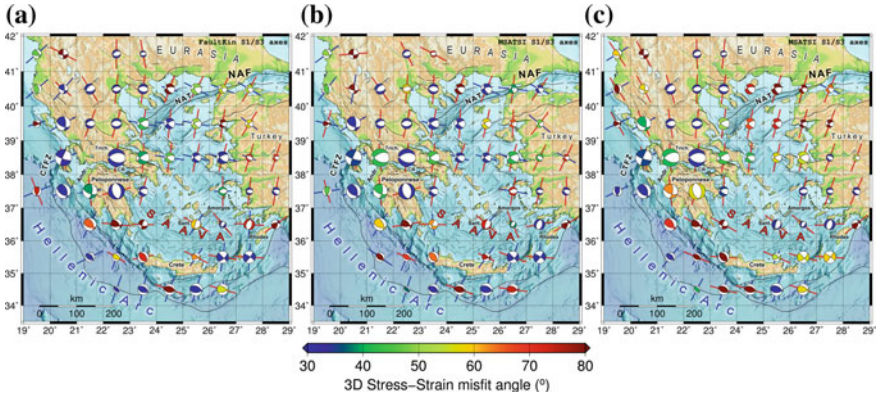

Fig. 19 Map of the resolved stress field using **a** FaultKin, **b** SATSI without damping and **c** SATSI with damping ($e=2$), where the blue and red lines represent the orientation of the compressional, $\mathbf{S}_1$, and extensional, $\mathbf{S}_3$, principal stress axes, respectively, with the length being reversely proportional to the corresponding axis' plunge. Beach-balls represent the expected focal mechanisms according to the strain field, as resolved by GPS measurements (Kreemer et al. 2014), interpolated to the point at the middle of each cell of Fig. 12. The color of the compressional P-wave first motion quadrant corresponds to the 3D misfit angle between stress and strain, using the method described in Sect. 5.1 for the minimum angular difference between two tensors. The beachballs' size is proportional to the logarithm of the number of available FMS data in each cell. SAAVA: South Aegean Active Volcanic Arc, Sant.: Santorini

from GSRM (http://gsrm2.unavco.org/model/model.html; Kreemer et al. 2014) for each cell and for different inversion methods or parameterizations. From this figure, one can note significant differences existing in numerous sub-regions, even in those cells for which robust results are thought to have been obtained. Those are mainly related to the issues discussed above and in the previous sections of the manuscript.

The stress ratio indicates uniaxial stress when it takes an extreme value such as $\Phi=1$ ($\sigma_2 \approx \sigma_1$) when $\mathbf{S}_3$ is generally stable but the same is not true for $\mathbf{S}_2$ and $\mathbf{S}_1$, with their values being comparable so that it isn't clear whether they should interchange. This also occurs for $\Phi=0$ ($\sigma_2 \approx \sigma_3$) where the maximum principal (compressive) stress, $\mathbf{S}_1$, is stable but $\mathbf{S}_3$ and $\mathbf{S}_2$ are not, resulting in comparable magnitudes. Even without stress inversion, this can be demonstrated by a distribution of **P** and **T** axis which indicates that e.g. despite a large RMS angular difference between FMS data and their average solution (such as the one derived by FaultKin; Fig. 13b), the **T** axis trend/plunge distribution has a generally small range, but this is not the case for the **P** axis, which is less stable.

The distribution of stress ratios ($\Phi=1-R$) are shown in Fig. 20. A good agreement is observed between FaultKin and un-damped SATSI, indicating that stresses tending towards uniaxial compression ($\Phi \rightarrow 0$, blue colors) are distributed mostly along the Hellenic Arc, while ratios corresponding to uniaxial extension ($\Phi \rightarrow 1$, red colors) or pure-shear ($\Phi \approx 0.5$, white colors) are mainly observed elsewhere. Un-damped SATSI yielded a different pattern in south Aegean related to uniaxial compression

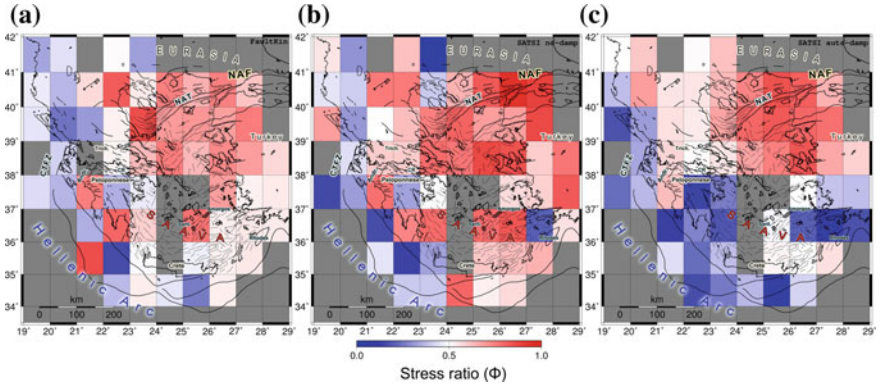

Fig. 20 Map of the resolved stress ratio (Φ) using **a** FaultKin, **b** SATSI without damping and **c** SATSI with damping ($e=2$), where the color scale blue-white-red indicates uniaxial compression ($\Phi=0$), pure-shear stress ($\Phi=0.5$) and uniaxial extension ($\Phi=1$). Grey colour denotes cells without data or solutions

instead of extension, which is likely the result of over-smoothing of the model. However, it is worth noting that reversal of stress shape occurs along the South Aegean Active Volcanic Arc (SAAVA). Since stress shape controls the orientations and magnitudes of tractions on the rupture surface, and thus it critically affects faults reactivation (Allmendinger et al. 2012), further research is needed on this issue.

Summarizing the abovementioned remarks, the following general conclusions can be drawn:

1. The resolving power of the methods is not directly related to the multitude of observations, but it is mainly connected with the data heterogeneity, basically inherent with complex tectonics.
2. Reversal of the stress field with respect to the strain field is frequently observed (i.e. large Kagan, or misfit angles), which is presumably an artifact of the respective stress model.
3. Given the distribution of the Kagan angles values, it is implied that FaultKin and un-damped SATSI procedure yielded consistent solutions for the largest part of the model.
4. The damped SATSI procedure failed to reproduce a robust regime for the largest part of the model due to over-damping. This does not reject the validity of the method but rather indicates that it is more dependent on proper data arrangement, likely into smaller, partially overlapping spatial cells or grouped into distinct source zones.
5. The methods are considered capable to efficiently resolve stresses when the criteria of the Wallace-Bott hypothesis and assumptions H_2, H_3 and H_4 are fulfilled, i.e. stress homogeneity over space and time and that input focal mechanisms are independent from each other. These issues are efficiently handled only by the MIM procedure. The other methods can perform satisfactorily only when the

data have been adequately pre-processed, specifically de-clustered and divided into subsets, the dimensions of which should be analogous to the ones of the involved structures.

6. Besides the aforementioned issues that require more caution in a future analysis, the results of this effort demonstrate that a separation of stress states occurs on either sides of the South Aegean Active Volcanic Arc (SAAVA), since the prominent $\mathbf{S_3}$ axes of tensional stress appear rotated by ~90°, oriented NW-SE. Hence, we could reasonably presume that this abrupt change, possibly related to crustal thinning along SAAVA due to the subduction process, is potentially the result of, or responsible for slab tearing in NE-SW (Sachpazi et al. 2016), or ~E-W (Jolivet et al. 2015) direction. However, a combination of geological-geophysical data is required to establish such a hypothesis.

Lastly, Table 4 summarizes the pros and cons of the three methods, as derived by their application to the FMS dataset in Greece. Some common issues include that the applied algorithms cannot take into account displacement data or the mechanical properties of the rupture surface. These are handled by the more advanced, third generation methods, also known as Geomechanical models (Sect. 3.3). However, they can provide useful insights into both the regional and local stress field in combination with ground displacement measurements.

Acknowledgements The map figures were drawn using the open-source Generic Mapping Tools (GMT) software (Wessel and Smith 1998; http://www.soest.hawaii.edu/gmt/).

Table 4 Summary of pros and cons of the methods used in this study

FaultKin	Pros	Simple, straightforward algorithm User friendly interface with high quality graphics and plenty of structural analysis capabilities Smaller RMS angular differences against the FMS dataset Easy to handle different input formats The focal mechanisms input follows the Aki-Richards convention Can perform slip tendency analysis given the regional stress field Compatible with other software on structural data analysis
	Cons	Time consuming: requires manual handling per dataset Unable to resolve highly heterogeneous data Uncertainties are large and cannot be quantified by the method Cannot resolve multiple stress states per dataset Output not easy to handle for other applications Unexpected behavior when imported P- and T-axes are not exactly perpendicular Does not ensure independency of focal mechanisms observations Negative eigenvalues (stress magnitudes) are unsigned in the output

(continued)

Table 4 (continued)

SATSI/MSATSI	Pros	Straightforward algorithm, can apply in the four dimensions (spatial and temporal domain) Un-damped solutions are similar to those of FaultKin, but likely more stable due to the resampling potential Smooth variations across the stress model Small uncertainties which are quantified through a resampling procedure Easy to apply (automatic application to grid) Takes into account the resolved stress states in neighboring cells Can resolve highly heterogeneous data, when properly arranged
	Cons	Requires manual handling of data preparation. Requires predefined a grid of cells, the configuration of which is subjective Large Φ uncertainties Cannot resolve multiple stress states per cell Over-smoothing due to damping can create artifacts Does not ensure independency of focal mechanisms observations The input does not follow the Aki-Richards convention, which is not practical when using focal mechanisms
MIM	Pros	Provides more insights into the distribution of the stress tensors Considers the effects of heterogeneity and faults interaction Quantified uncertainties in terms of model-data misfit angles Reduction of redundant and erroneous data Discrimination between different stress states in the same set of data Narrow Φ filtering is possible The focal mechanisms input follows the Aki-Richards convention Nodal planes ambiguity is eliminated since both nodal planes are considered independently by resampling Can perform slip tendency analysis given a regional stress field
	Cons	Complex theoretical background that may be difficult for beginners Time consuming input preparation Requires manual handling per dataset Computational performance requirements increase with the number of observations Only a limited number of observations can be analyzed by the available 32bit version of the code Low graphics resolution, not suitable for publication; complementary graphics software is prerequisite Output not easy to handle for other applications

References

Aki K, Patton H (1978) Determination of seismic moment tensor using surface waves. Tectonophysics 49:213–222

Aki K, Richards PG (2002) Quantitative seismology. University Science Books, USA

Aleksandrowski P (1985) Graphical determination of principal stress directions for slickenside lineation populations: an attempt to modify Arthaud's method. J Struct Geol 7:73–82

Allmendinger RW (1989) Notes on fault slip analysis. In: Short course on quantitative interpretation of joints and faults. Geological Society of America Boulder CO, 59 pp

Allmendinger RW (2016) FaultKin 75 for Mac OS X Windows and Linux. User's Manual, 31 pp

Allmendinger RW, Cardozo N, Fisher D (2012) Structural geology algorithms: vectors and tensors in structural geology. Cambridge University Press. ISBN-13: 978–0748754755, p 290

Allmendinger RW, Gephart JW, Marrett RA (1989) Quantitative interpretation of joints and faults. In: Short course on quantitative interpretation of joints and faults. Geological Society of America Boulder CO, 59 pp

Anderson EM (1905) The dynamics of faulting. Trans Edinb Geol Soc 8:387–402

Anderson EM (1951) The dynamics of faulting and dyke formation with applications to Britain, 2nd edn. Oliver and Boyd Edinburgh

Angelier J (2002) Inversion of earthquake focal mechanisms to obtain the seismotectonic stress IV—A new method free of choice among nodal lines. Geophys J Int 150:588–609

Angelier J, Slunga R, Bergerat F, Stefansson R, Homberg C (2004) Perturbation of stress and oceanic rift extension across transform faults shown by earthquake focal mechanisms in Iceland. Earth Planet Sci Lett 219:271–284

Angelier J (1989) From orientation to magnitudes in paleostress determination using fault slip data. J Struct Geol 11:37–50

Angelier J (1979) Determination of the mean principal directions of stresses for a given fault population. Tectonophysics 56:T17–T26

Angelier J (1984) Tectonic analysis of fault slip data sets. J Geophys Res 89:5835–5848

Angelier J, Tarantola A, Valette B, Manoussis S (1982) Inversion of field data in fault tectonics to obtain the regional stress I Single phase fault populations: a new method of computing the stress tensor. Geophys J R Astron Soc 69:607–621

Angelier J, Mechler P (1977) Sur une methode graphique de recherche des contraintes principales egalment utilisable en tectonique et en seismologie: La methode des diedres droits. Bull Soc Geol Fr 19:1309–1318

Armijo R, Carey E, Cisternas A (1982) The inverse problem in microtectonics and the separation of tectonic phases. Tectonophysics 82:145–160

Arthaud F (1969) Méthode de détermination graphique des directions de raccourcissement d'allongement et intermédiare d'une population de failles. Bull Soc Géol Fr 11:729–737

Barth A, Reinecker J, Heidbach O (2008) World Stress Map project guidelines: stress derivation from earthquake focal mechanisms. GFZ-Potsdam Potsdam Germany

Bernard P, Zollo A (1989) Inversion of near-source S polarization for parameters of double couple point like sources. Bull Seism Soc Am 79:1779–1809

Bingham C (1964) Distributions on the sphere and on the projective plane. PhD Dissertation, Yale University, New Haven, CT

Bingham C (1974) An antipodally symmetric distribution on the sphere. Ann Stat 2:1201–1225

Bock Y, Melgar D (2016) Physical applications of GPS geodesy: a review. Rep Prog Phys 79:119 pp

Bogiatzis P, Ishii M (2014) Constraints on the moment tensor of the 2011 Tohoku-Oki earthquake from earth's free oscillations. Bull Seismol Soc Am 104:875–884

Bott MHP (1959) The mechanics of oblique slip faulting. Geol Mag 96:109–117

Bürgmann R, Pollard D, Martel S (1994) Slip distributions on faults: effects of stress gradients inelastic deformation heterogeneous host-rock stiffness and fault interaction. J Struct Geol 16:1675–1688

Byerlee J (1978) Friction of rocks. Pure Appl Geophys 116:615–626
Carey E, Brunier B (1974) Analyse théorique et numérique d'un modèle mécanique élémentaire applequé à l'étude d'une population de failles. C R Hebd Séanc Acad Sci Paris D 279:891–894
Célérier B (1988) Constraint on stress tensor from slip on a single fault plane. University of Texas at Austin Institute for Geophysics, Technical report No 73, 88 pp
Célérier B (2010) Remarks on the relationship between the tectonic regime the rake of the slip vectors the dip of the nodal planes and the plunges of the P, B, T-axes of earthquake focal mechanisms. Tectonophysics 482:1042–1049
Choi P-Y, Angelier J, Souffache´ B (1996) Distribution of angular misfits in fault-slip data. J Struct Geol 18:1353–1367
Chousianitis K, Ganas A, Evangelidis CP (2015) Strain and rotation rate patterns of mainland Greece from continuous GPS data and comparison between seismic and geodetic moment release. J Geophys Res Solid Earth 120(5):3909–3931
Compton RR (1966) Analysis of Pliocene-Pleistocene deformation and stresses in northern Santa Lucia Range California. Geol Soc Am Bull 77:1361–1380
Dahlen FA, Tromp J (1998) Theoretical global seismology. Princeton University Press pp 944
Dahm T, Krüger F (2014) Moment tensor inversion and moment tensor interpretation. Information Sheet IS39
Delvaux D, Sperner B (2003) Stress tensor inversion from fault kinematic indicators and focal mechanism data: the TENSOR program. In: Nieuwland D (ed), New insights into structural interpretation and modelling, vol 212. Special Publications, Geological Society, London, pp 75–100
Dufumier H (1996) On the limits of linear moment tensor inversion of teleseismic body wave spectra. Pageoph 147:467–482
Dufumier H, Cara M (1995) On the limits of linear moment tensor inversion of surface wave spectra. Pageoph 145:235–257
Eberhart-Phillips D (1986) Three-dimensional velocity structure in northern California coast ranges from inversion of local earthquake arrival times. Bull Seismol Soc Am 76:1025–1052
Etchecopar A, Vasseur G, Daignieres M (1981) An inverse problem in microtectonics for the determination of stress tensors from fault striation analysis. J Struct Geol 3:51–65
Fry N (1999) Striated faults: visual appreciation of their constraint on possible paleostress tensors. J Struct Geol 21:7–21
Ganas A, Drakatos G, Pavlides SB, Stavrakakis GN, Ziazia M, Sokos E, Karastathis VK (2005) The 2001 Mw = 64 Skyros earthquake conjugate strike-slip faulting and spatial variation in stress within the central Aegean Sea. J Geodyn 39:61–77
Gapais D, Cobbold PR, Bourgeois O, Rouby D, De Urreiztieta M (2000) Tectonic significance of fault-slip data. J Struct Geol 22:881–888
Gasperini P, Vannucci G (2003) FPSPACK: a package of FORTRAN subroutines to manage earthquake focal mechanism data. Comput Geosci 29:893–901
Gephart JW, Forsyth DW (1984) An improved method for determining the regional stress tensor using earthquake focal mechanism data: application to the San Fernando earthquake sequence. J Geophys Res 89:9305–9320
Gephart JW (1985) Principal stress directions and the ambiguity in fault plane identification from focal mechanisms. Bull Seismol Soc Am 75:621–625
Gephart JW (1988) On the use of stress inversion of fault-slip data to infer the frictional strength of rocks. EOS Am Geophys Union Trans 69:1462
Gephart JW (1990) Stress and the direction of slip on fault planes. Tectonophysics 8:845–858
Godano M, Deschamps A, Lambotte S, Lyon-Caen H, Bernard P, Pacchiani F (2014) Focal mechanisms of earthquake multiplets in the western part of the Corinth rift (Greece): influence of the velocity model and constraints on the geometry of the active faults. Geophys J Int 197:1660–1680
GSRM. http://gsrm2.unavco.org/model/model.html. Accessed April 2017
Hardebeck JL, Hauksson E (2001) Stress orientations obtained from earthquake focal mechanisms: what are appropriate uncertainty estimates. Bull Seism Soc Am 91(2):250–262

Hardebeck JL, Michael AJ (2006) Damped regional-scale stress inversions: methodology and examples for southern California and the Coalinga aftershock sequence. J Geophys Res 111:B11310
Haslinger F, Kissling E, Ansorge J, Hatzfeld D, Papadimitriou E, Karakostas V, Makropoulos K, Kahle H-G, Peter Y (1999) 3D crustal structure from local earthquake tomography around the Gulf of Arta (Ionian region NW Greece). Tectonophysics 304:201–218
Hatzfeld D, Kassaras I, Panagiotopoulos DG, Amorese D, Makropoulos K, Karakaisis GF, Coutant O (1995) Microseismicity and strain pattern in Northwestern Greece. Tectonics 14:773–785
Heidbach OJ, Reinecker M, Tingay B, Müller B, Spencer K, Fuchs F, Wenzel (2007) Plate boundary forces are not enough: Second- and third-order stress patterns highlighted in the World Stress Map database. Tectonics 26(6):TC6014
Heidbach O, Rajabi M, Reiter K, Ziegler M (2016) World Stress Map 2016. GFZ Data Services. https://doi.org/10.5880/WSM.2016.002
Heidbach O, Tingay M, Barth A, Reinecker J, Kurfeß D, Müller B (2010) Global crustal stress pattern on the World Stress Map database release 2008. Tectonophysics 482:3–15
Herrmann RB, Ammon CJ (1997) Faulting parameters of earthquakes in the New Madrid, Missouri, region. Eng Geol 46:299–311
Huang Q (1988) Computer-based method to separate heterogeneous sets of fault-slip data into sub-sets. J Struct Geol 10:297–299
Jackson J, McKenzie D (1988) The relationship between plate motions and seismic moment tensors and the rates of active deformation in the Mediterranean and Middle East. Geophys J 93(88):46–73
Jolivet L, Menant A, Sternai P, Rabillard A, Arbaret L, Augier R, Laurent V, Beaudoin A, Bernhard A, Grasemann B, Huet B, Labrousse L, Le Pourhiet L (2015) The geological signature of a slab tear below the Aegean. Tectonophysics 659:166–182
Julien PH, Cornet FH (1987) Stress determination from aftershocks of the Campania-Lucania earthquake of November 23 1980. Ann Geophys 5B(3):289–300
Kabsch W (1978) A discussion of the solution for the best rotation to relate two sets of vectors. Acta Crystallogr Sect A(34):827–828
Kagan YY (1991) 3-D rotation of double-couple earthquake sources. Geophys J Int 106:709–716
Kamb WB (1959) Ice petrofabric observations from Blue Glacier Washington in relation to theory and experiment. J Geophys Res 64:1891–1909
Kapetanidis V (2017) Spatiotemporal patterns of microseismicity for the identification of active fault structures using seismic waveform cross-correlation and double-difference relocation. PhD Thesis, National and Kapodistrian University of Athens
Kapetanidis V, Deschamps A, Papadimitriou P, Matrullo E, Karakonstantis A, Bozionelos G, Kaviris G, Serpetsidaki A, Lyon-Caen H, Voulgaris N, Bernard P, Sokos E, Makropoulos K (2015) The 2013 earthquake swarm in Helike Greece: seismic activity at the root of old normal faults. Geophys J Int 202:2044–2073
Karakonstantis A, Papadimitriou P (2010) Earthquake relocation in Greece using a unified and homogenized seismological catalogue. Bulletin of the Geological Society of Greece, Proceedings of the 12th International Congress XLIII(4):2043–2052
Kassaras I, Kapetanidis V, Karakonstantis A (2016a) On the spatial distribution of seismicity and the 3D tectonic stress field in western Greece. Phys Chem Earth 95:50–72
Kassaras I, Kapetanidis V, Karakonstantis A, Ganas A (2016b) Regional patterns of earthquake sources in Western Greece: Insights on the 3-D stress tensor and seismic velocity structure arrangement. Paper presented in the General Assembly of the ESC, 4–10 September 2016, Trieste, Italy, paper no 556
Kassaras I, Kapetanidis V, Karakonstantis A, Kaviris G, Papadimitriou P, Voulgaris N, Makropoulos K, Popandopoulos G, Moshou A (2014a) The April–June 2007 Trichonis Lake earthquake swarm (W Greece): New implications toward the causative fault zone. J Geodyn 73:60–80
Kassaras I, Kapetanidis V, Karakonstantis A, Kouskouna V, Ganas A, Chouliaras G, Drakatos G, Moshou A, Mitropoulou V, Argyrakis P, Lekkas E, Makropoulos K (2014b) Constraints on the dynamics and spatio-temporal evolution of the 2011 Oichalia seismic swarm (SW Peloponnesus Greece). Tectonophysics 614:100–127

Kassaras I, Karakonstantis A, Vlachou K, Kapetanidis V, Kaviris G, Papadimitriou P, Voulgaris N, Lagios E, Makropoulos K (2012) Study of the Geodynamics in Aitoloakarnania (W Greece) based on joint Seismological and GPS. In: Paper presented in the 33rd ESC general assembly Moscow Russia, pp 164–165

Kassaras I, Karakonstantis A, Vlachou K, Kapetanidis V, Kaviris G, Vlachou K, Papadimitriou P, Voulgaris N, Makropoulos K (2013) On the geodynamics of western Greece deduced by massive seismological observations. Paper presented in the AHS/IAPSO/IASPEI joint assembly, Gothenburg, Sweden, 22–26 July 2013

Kassaras I, Louis F, Makropoulos K, Magganas A, Hatzfeld D (2009) Elastic-Anelastic properties of the Aegean Lithosphere-Asthenosphere inferred from long period rayleigh waves. In: Anderson JE, Coates RW (eds) The Lithosphere: geochemistry geology and geophysics. Nova Publishers, NY, USA, pp 267–294. ISBN: 978-1-60456-903-2

Kaven JO, Maerten F, Pollard DD (2011) Mechanical analysis of fault slip data: implications for paleostress analysis. J Struct Geol 33:78–91

Konstantinou KI, Mouslopoulou V, Liang W-T, Heidbach O, Oncken O, Suppe J (2017) Present-day crustal stress field in Greece inferred from regional-scale damped inversion of earthquake focal mechanisms. J Geophys Res Solid Earth 122:506–523

Kreemer C, Blewitt G, Klein EC (2014) A geodetic plate motion and global strain rate model. Geochem Geophys Geosyst 15:3849–3889

Laigle M, Hirn A, Sachpazi M, Clément C (2002) Seismic coupling and structure of the Hellenic subduction zone in the Ionian islands region. Earth Planet Sci Lett 200:243–253

Leavers VF (1992) Shape detection in computer vision using the hough transform. Springer, London

Lejri M (2015) Subsurface stress inversion modeling using linear elasticity: sensitivity analysis and applications. PhD Thesis, Geophysics [physicsgeo-ph] Universite de Montpellier pp 317 (https://hal.archives-ouvertes.fr) HAL Id: tel-01324110 version 1

LePichon X, Angelier J (1979) The Hellenic arc and trench system: a key to the neotectonic evolution of the Eastern Mediterranean area. Tectonophysics 60:1–42

Lisle RJ (1987) Principal stress orientations from faults: an additional constraint. Ann Tecton 1:155–158

Lund B, Slunga R (1999) Stress tensor inversion using detailed microearthquake information and stability constraints: application to Olfus in southwest Iceland. J Geophys Res 104:14947–14964

Lyon-Caen H, Armijo R, Drakopoulos J, Baskoutass J, Delibassis N, Gaulon R, Kouskouna V, Latoussakis J, Makropoulos K, Papadimitriou P, Papanastassiou D, Pedotti G (1988) The 1986 Kalamata (South Peloponnesus) earthquake: detailed study of a normal fault evidences for east-west extension in the Hellenic Arc. J Geophys Res Solid Earth 93:14967–15000

Maerten F, Maerten L, Cooke M (2010) Solving 3D boundary element problems using constrained iterative approach. Comput Geosci 14(4):551–564

Maerten F, Resor PG, Pollard DD, Maerten L (2005) Inverting for slip on three-dimensional fault surfaces using angular dislocations. Bull Seismol Soc Am 95:1654–1665

Makropoulos K, Diagourtas D, Kassaras J, Kouskouna V, Papadimitriou P, Ziazia M (1996) The November–December 1994 Lefkas (W Greece) earthquake sequence: results from in situ seismological survey. In: Book of abstracts XXV general assembly of ESC, Reykavik, Iceland, p 108

Mariolakos I, Papanikolaou D (1987) Deformation pattern and relation between deformation and seismicity in the Hellenic arc. Bull Geol Soc Greece (in Greek) XIX:59–76

Marrett RA, Allmendinger RW (1990) Kinematic analysis of fault-slip data. J Struct Geol 12:973–986

Martel S, Shacat C (2006) Mechanics and interpretations of fault slip. In: Abercrombie R, DiToro G, Kanamori H, McGarr A (eds) Radiated energy and the physics of earthquake faulting, vol 170. American Geophysical Union Monograph, pp 207–216

Martínez-Garzón P, Kwiatek G, Ickrath M, Bohnhoff M (2014) MSATSI: A MATLAB package for stress inversion combining solid classic methodology anew simplified user-handling and a visualization tool. Seismol Res Lett 85(4):896–904

Maury JFH, Cornet F, Dorbath L (2013) A review of methods for determining stress fields from earthquake focal mechanisms: application to the Sierentz 1980 seismic crisis (Upper Rhine graben). Bull Soc Geol Fr 184:319–334

McKenzie DP (1969) The relation between fault plane solutions for earthquakes and the directions of the principal stresses. Bull Seism Soc Am 59:591–601

McKenzie DP (1972) Active tectonics of the Mediterranean region. Royal Astron Soc Geophys J 30:109–182

Menke W (1984) Geophysical data analysis: discrete inverse theory. Academic Press, Orlando, Florida

Mercier JL, Carey-Gailhardis E (1989) Regional state of stress and characteristic fault kinematics instabilities shown by aftershock sequences: the aftershock sequences of the 1978 Thessaloniki (Greece) and 1980 Campania-Lucania (Italia) earthquakes as examples. Earth Planet Sci Lett 92(2):247–264

Michael AJ (1984) Determination of stress from slip data: faults and folds. J Geophys Res 89:11517–11526

Michael AJ (1987) Use of focal mechanisms to determine stress: a control study. J Geophys Res 92:357–368

Michael AJ (1991) Spatial variations in stress within the 1987 Whittier Narrows California aftershock sequence: new techniques and results. J Geophys Res 96:6303–6319

Milano G, Di Giovambattista R (2011) Seismicity at the border between Central and Southern Apennines (Italy): re-evaluation of the early 1984 instrumental earthquake. Tectonophysics 499:92–104

Molnar P (1983) Average regional strain due to slip on numerous faults of different orientations. J Geophys Res 88:6430–6432

Muller OH, Pollard DD (1977) The state of stress near Spanish Peaks Colorado determined from a dike pattern. Pure Appl Geophys 115:69–86

Okada Y (1992) Internal deformation due to shear and tensile faults in a half-space. Bull Seismol Soc Am 82(2):1018–1040

Ortner H, Reiter F, Acs P (2002) Easy handling of tectonic data: the programs TectonicVB for Mac and TectonicsFP for Windows. Comput Geosci 28:1193–1200

Otsubo M, Yamaji A (2006) Improved resolution of the multiple inverse method by eliminating erroneous solutions. Comput Geosci 32:1221–1227

Otsubo M, Sato K, Yamaji A (2006) Computerized identification of stress tensors determined from heterogeneous fault-slip data by combining the multiple inverse method and k-means clustering. J Struct Geol 28:991–997

Otsubo M, Yamaji A, Kubo A (2008) Determination of stresses from heterogeneous focal mechanism data: an adaptation of the multiple inverse method. Tectonophysics 457:150–160

Papadimitriou P, Kassaras I, Rigo A, Lyon-Caen H, Hatzfeld D, Makropoulos K, Drakopoulos J (1994) Source parameters of large and small earthquakes in Corinth Gulf (C. Greece) In: Proceedings of the XXIV general assembly of the ESC, pp 848–858

Papanikolaou ID, Papanikolaou DI, Lekkas EL (2009) Advances and limitations of the environmental seismic intensity scale (ESI 2007) regarding near-field and far-field effects from recent earthquakes in Greece: implications for the seismic hazard assessment. In: Reicherter K Michetti AM, Silva PG (eds) Palaeoseismology: historical and prehistorical records of earthquake ground effects for seismic hazard assessment, vol 316. Geological Society of London, Special Publications, pp 11–30

Papazachos B, Papazachou C (2003) The earthquakes of Greece, 3rd edn. Ziti Public Thessaloniki

Pérouse E, Sébrier M, Braucher R et al (2016) Transition from collision to subduction in Western Greece: the Katouna-Stamna active fault system and regional kinematics. Int J Earth Sci (Geol Rundsch) 106(3):967–989

Philippson A (1998) La tectonique de l' Egeide. Ann Geogr 112–141

Plateaux R, Angelier J, Bergerat F, Cappa F, Stefánsson R (2010) Stress changes induced at neighboring faults by the June 2000 earthquakes South Iceland seismic zone. Terra Nova 22:79–86

Pollard DD, Saltzer SD (1993) Stress inversion methods: are they based on faulty assumptions? J Struct Geol 15:1045–1054
Pollard D, Segall P (1987) Theoretical displacements and stresses near fractures in rock: with applications to faults joints veins dikes and solution surfaces. In: Atkinson B (ed) Fracture mechanics of rocks. Academic Press, San Diego
Reches Z (1987) Determination of the tectonic stress tensor from slip along faults that obey the Coulomb yield condition. Tectonics 6:849–861
Reches Z, Baer G, Hatzor Y (1992) Constraints on the strength of the upper crust from stress inversion of fault slip data. J Geophys Res 97:12481–12493
Richardson RM (1992) Ridge forces absolute plate motions and the intraplate stress field. J Geophys Res 97:11739–11748
Rigo A, Lyon-Caen H, Armijo R, Deschamps A, Hatzfeld D, Makropoulos K, Papadimitriou P, Kassaras I (1996) A microseismic study in the western part of the Gulf of Corinth (Greece): implications for large-scale normal faulting mechanisms. Geophys J Int 126:663–688
Royden LH, Papanikolaou DJ (2011) Slab segmentation and late Cenozoic disruption of the Hellenic arc. Geochem Geophys Geosyst 12(3):Q03010
Sachpazi M, Laigle M, Charalampakis M, Diaz J, Kissling E, Gesret A, Becel A, Flueh E, Miles P, Hirn A (2016) Segmented Hellenic slab rollback driving Aegean deformation and seismicity. Geophys Res Lett 43(2). https://doi.org/10.1002/2015gl066818
Sakellariou D, Tsampouraki-Kraounaki K (2016) Offshore faulting in the Aegean Sea: a synthesis based on bathymetric and seismic profiling data. In: Bulletin of the Geological Society of Greece, Proceedings of the 14th International Congress, Thessaloniki, May 2016
Scholz CH (2002) The mechanics of earthquakes and faulting. Cambridge Press, ISBN: 1107079039
Segall P, Pollard D (1980) Mechanics of discontinuous faults. J Geophys Res 85:4337–4350
Serpetsidaki A, Elias P, Ilieva M, Bernard P, Briole P, Deschamps A, Lambotte S, Lyon-Caen H, Sokos E, Tselentis G-A (2014) New constraints from seismology and geodesy on the Mw = 64 2008 Movri (Greece) earthquake: evidence for a growing strike-slip fault system. Geophys J Int 198:1373–1386
Shan Y, Li Z, Lin G (2004) A stress inversion procedure for automatic recognition of polyphase fault/slip data sets. J Struct Geol 26(5):919–925
Shuster MD (1993) A survey of attitude representations. J Astronaut Sci 41(4):439–517
Sperner BB, Müller O, Heidbach D, Delvaux J, Reinecker K, Fuchs K (2003) Tectonic stress in the Earth's crust: advances. In: Nieuwland DA (ed) The World Stress Map project: New insights in structural interpretation and modeling, London Geological Society, pp 101–116
Stein S, Wysession M (2003) An introduction to seismology earthquakes and earth structure. Blackwell, Malden, MA, 510 pp. ISBN: 978-0-86542-078-6
Stucchi M, Rovida A, Gomez Capera AA, Alexandre P, Camelbeeck T, Demircioglu MB, Gasperini P, Kouskouna V, Musson RMW, Radulian M, Sesetyan K, Vilanova S, Baumont D, Bungum H, Fäh D, Lenhardt W, Makropoulos K, Martinez-Solares JM, Scotti O, Živčić M, Albini P, Batllo J, Papaioannou C, Tatevossian R, Locati M, Meletti C, Viganò D, Giardini D (2013) The SHARE European Earthquake catalog (SHEEC) 1000-1899. J Seismol 17(2):523–544
Tape W, Tape C (2012) Angle between principal axis triples. Geophys J Int 108:813–831
Thomas AL (1993) Poly3D: a three-dimensional polygonal-element displacement discontinuity boundary element computer program with applications to fractures faults and cavities in the Earth's crust. MSc thesis, Stanford University, California
Tibi R, Bock G, Xia Y, Baumbach M, Grosser H, Milkereit C, Karakisa S, Zünbül S, Kind R, Zschau J (2001) Rupture processes of the 1999 August 17 Izmit and November 12 Düzce (Turkey) earthquakes. Geophys J Int 144(2):F1–F7
Toda SR, Stein V, Sevilgen, Lin J (2011) Coulomb 33 graphic-rich deformation and stress-change software for earthquake tectonic and volcano research and teaching-user guide. US Geological Survey, Open File Report 2011-1060, 54 pp
Turcotte DL, Schubert G (2002) Geodynamics, 3rd edn. Cambridge University Press

Twiss RJ, Unruh JR (1998) Analysis of fault slip inversions: do they constrain stress or strain rate? J Geophys Res 103(B6):12205–12222
Vavryčuk V (2014) Iterative joint inversion for stress and fault orientations from focal mechanisms. Geophys J Int 199(1):69–77
Vavryčuk V (2015) Earthquake mechanisms and stress field. In: Encyclopedia of earthquake engineering. Springer, Berlin. https://doi.org/10.1007/978-3-642-36197-5_295-1
Vvedenskaya AV (1956) Determination of displacement fields in earthquakes with the aid of dislocation theory. Bull Acad Sci USSR 3:1956
Wallace RE (1951) Geometry of shearing stress and relation to faulting. J Geol 59:118–130
Wessel P, Smith WHF (1998) New improved version of generic mapping tools released. Eos Trans Am Geophys Union 79:579–579
Wiemer S (2001) A software package to analyze seismicity: ZMAP. Seismol Res Lett 72:373–382
Yamaji A (2000) The multiple inverse method: a new technique to separate stresses from heterogeneous fault-slip data. J Struct Geol 22:441–452
Yamaji A (2016) Genetic algorithm for fitting a mixed Bingham distribution to 3D orientations: a tool for the statistical and paleostress analyses of fracture orientations. Island Arc 25:72–83
Yamaji A, Otsubo M, Sato K (2006) Paleostress analysis using the Hough transform for separating stresses from heterogeneous fault-slip data. J Struct Geol 28:980–990
Yamaji A, Sato K (2011) A spherical code and stress tensor inversion. Comput Geosci 38(1):164–167. https://doi.org/10.1016/j.cageo.2011.04.016
Yamaji A, Sato K, Otsubo M (2011) Multiple inverse method user's manual © 2004, pp 42
Zoback ML (1992) First- and second-order patterns of stress in the lithosphere: The World Stress Map project. J Geophys Res 97:11703–11728
Zoback ML, Zoback MD, Adams J, Assumpção M, Bell S, Bergman E, Blümling P, Brereton NR, Denham D, Ding J, Fuchs K, Gay N, Gregersen S, Gupta HK, Gvishiani A, Jacob K, Klein R, Knoll P, Magee M, Mercier JL, Müller BC, Paquin C, Rajendran K, Stephansson O, Suarez G, Suter M, Udias A, Xu Zh, Zhizhin M (1989) Global patterns of tectonic stress. Nature 341:291–298